12-2015

Dark Matter Halo Concentration and the Evolution of Spiral Structure in N-Body, Barred Spiral Galaxies

Jazmin Esmeralda Berlanga Medina
University of Arkansas, Fayetteville

Dark Matter Halo Concentration and the Evolution of Spiral Structure in N-Body, Barred Spiral Galaxies

A thesis submitted in partial fulfillment
of the requirements for the degree of
Master of Science in Physics

by

Jazmin Esmeralda Berlanga Medina
University of Arkansas
Bachelor of Science in Physics, 2010

December 2015
University of Arkansas

This thesis is approved for recommendation to the Graduate Council.

Dr. Daniel Kennefick
Thesis Director

Dr. Julia Kennefick
Committee Member

Dr. Mark Arnold
Committee Member

Dr. Salvador Barraza-Lopez
Committee Member

Abstract

Motivated by the evidence of relationships between pitch angle (the tightness of spiral arm structure in the disk), P, and various indicators of central mass concentration, as well as the theoretical relationship between halo mass concentration and the density of visible matter in the central part of the galaxy, we look at a possible relationship between P and c_{vir} (the virial concentration of the dark matter halo) in N-body simulations of barred, spiral galaxies. We also look at the evolution of pitch angle over time in higher temporal resolution than any data currently available in the literature. We find that pitch angle structure is recurring, the overall distribution staying within a relatively narrow range. We do not find evidence for a relation between P and c_{vir}.

Acknowledgements

A huge thanks to...

My advisor, Dr. Daniel Kennefick, for mentoring me in two thesis projects towards both a bachelor's and master's degree. Dr. Joel Berrier, for his critical role in getting this project off the ground and continued support even after leaving Arkansas. My committee, Dr. Mark Arnold, Dr. Julia Kennefick and Dr. Salvador Barraza-Lopez. Thank you all, for all the time you've invested in me.

Jeff Pummill, Dr. David Chaffin, Dr. Pawel Wolinski and the Arkansas High Performance Computing Center (AHPCC), supported in part by the National Science Foundation (NSF) under grants MRI #0722625, MRI-R2 #0959124 and MRI-R2 #0918970, for the use of their computing resources and extremely helpful user support. The Extreme Science and Engineering Discovery Environment (XSEDE), supported by the National Science Foundation under grant ACI-1053575, for providing computing hours (allocation TG-AST140017) on the Gordon super-computer at the San Diego Supercomputer Center (SDSC), which were used to perform a second set of simulations that I was not able to use in this work.

Erik Monson, current Physics undergraduate, for his work on measuring a portion of the pitch angle data presented here, and his huge contribution to 2DFFT Utilities. Matt Hartley, former Physics undergraduate, for his overall IT support, programming help when I was just getting started and analysis of early iterations of simulation data that, while ultimately not used, was helpful in defining this project.

My research group, the Arkansas Galaxy Evolution Survey (AGES), the Physics Department, the Graduate School and the Arkansas Center for Space and Planetary Sciences (SPAC) for financial support in attending conferences to present earlier versions of this work, as well as countless other contributions.

Judy and Bill Schwab, for finding the financial resources for this DREAMer go to grad school when my immigration status made it impossible to work. William Oliver III, my undergraduate academic advisor, and his wife, Debbie Oliver, for their optimism and support, which were a very important part of my time in Fayetteville.

Amanda, Kim, Sara, Doug and everyone else who's been a much-needed friend throughout grad school–you are amazing and will go very, very far.

My family: Mom, Diana and Frankc. Los quiero mucho.

Ben, Scruffy and Zwicky. I love you. <3

Table of Contents

List of Figures

List of Tables

1 Introduction

The evolution of galaxies is an area of study that has puzzled and fascinated astronomers since they began to put together a model of our own Milky Way galaxy a century ago. The variety of galactic structure seen in the Universe today poses both an observational challenge and an opportunity to make new discoveries with ever-improving tools, such as next-generation telescopes (e.g., the James Webb Space Telescope) and N-body simulations of increasing particle numbers and physical accuracy (made possible as computational hardware and software evolves).

Spiral galaxies in particular are complex, involving physical processes that operate at the smallest of scales—for instance, the nucleo-chemistry of star birth and death—and the large scale—the gravitational interaction of dark matter and global galactic structure. Much of what we know about galaxies comes from probing the large-scale structures and forces that form them, but we still have many fundamental questions left unanswered.

Here, we look at one particular aspect of the connection between dark matter and spiral structure. Motivated by the evidence of relationships between pitch angle (the tightness of spiral arm structure in the disk), P, and various indicators of central mass concentration, as well as the theoretical relationship between halo mass concentration and the density of visible matter in the central part of the galaxy, we look at a possible relationship between P and c_{vir} (the virial concentration of the dark matter halo) in N-body simulations of barred, spiral galaxies. We also look at the evolution of pitch angle over time in higher temporal resolution than any data currently available in the literature.

This paper is organized as follows: Chapter 2 contains theoretical background on spiral structure formation, pitch angle, and dark matter halos. Chapter 3 contains a description of our model galaxies and methodologies. We discuss results in Chapter 4 and their implications in Chapter 5.

2 Background

2.1 Spiral Galaxies

Most people know spiral galaxies by the widely-publicized images of grand design spirals. These galaxies are characterized by the presence of two, symmetric arms, with either a circular bulge (Figure 2.1) or a linear bar (Figure 2.2) in the middle–or sometimes a structure with characteristics of both.

Figure 2.1: An example of a grand design spiral galaxy (M81) with a bulge in the center. Image from Wikipedia (2014b), credit NASA and the Spitzer Space Telescope (SSC & Caltech).

In all galaxy types, the arms tend to be brighter and bluer than the rest of a galaxy's disk due to the abundance of star-forming regions. This indicates a relatively young stellar population. The oldest, reddest stars reside in the galactic center (and also in areas of the disk that are no longer conducive to star formation).

Galaxies also have an interstellar medium composed mostly of gas and dust. A dark matter halo (which does not emit any sort of radiation and is therefore not directly visible) encompasses the entire galaxy and extends radially far beyond the visible components.

Grand design spirals are just one of many morphological types. The basic morphological categories were famously organized by Edwin Hubble into the "tuning fork" classification

Figure 2.2: An example of a grand design spiral galaxy with a bar at the center (NGC 1300). Image from Wikipedia (2015a), credit NASA, HST & ESA.

scheme (Hubble, 1926; Carroll & Ostlie, 2006). This "fork", sometimes known as the Hubble Sequence, is pictured in Figure 2.3. Ellipticals are shown on the "handle" with spirals on the "prongs". Spirals are further divided into those with bulges and those with bars. Those with larger bulges/bars and tighter arms are closer to the handle. Irregular galaxies (such as the one in Figure 2.4), are usually placed at the end opposite the ellipticals.

Early on, Hubble and others mistakenly identified elliptical galaxies as being the evolutionary pre-cursors to spiral galaxies (Carroll & Ostlie, 2006, chapter 25). That is, they thought that ellipticals changed into spiral galaxies over time, diverging into barred and non-barred populations. This led to the nomenclature we still use today–"early-type" for elliptical and "late-type" for spiral galaxies.

Today, we know that spiral galaxies formed early on in the history of the Universe. Other aspects of the tuning fork are also being exposed to scrutiny. Some astronomers contend that the binary bulge/bar paradigm is too simplistic. They argue that the exact shape and nature of the structure that makes up the center of galaxies exists along a continuum, with strictly-defined bulges and bars at opposite ends. Work by Gérard de Vaucouleurs, among others, has resulted in modified tuning fork schemes such as the one in Figure 2.5.

2.1.1 Spiral Structure Formation Theories

Ideally, classifying galaxies should help us understand how they evolve. Modern classification schemes give some indication of how to divide up galaxies into populations, but are of little help in understanding the mechanisms that drive galaxy formation. The topic of galaxy evolution in general has several, fundamental questions that are still open,

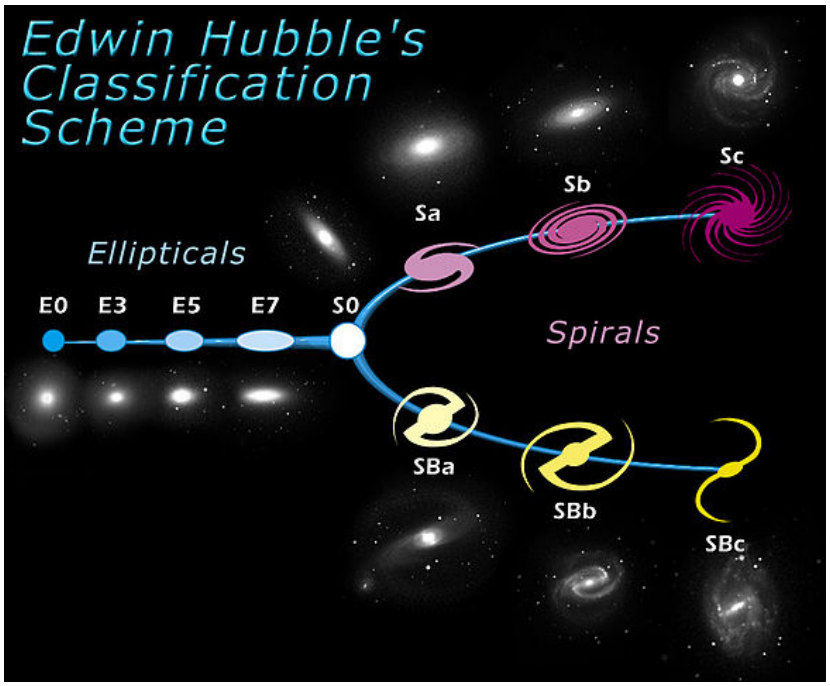

Figure 2.3: Edwin Hubble's "tuning fork" for galaxy morphology classification, including observational images that demonstrate the various types. Image from Wikipedia (2015d), based off work in Hubble (1926).

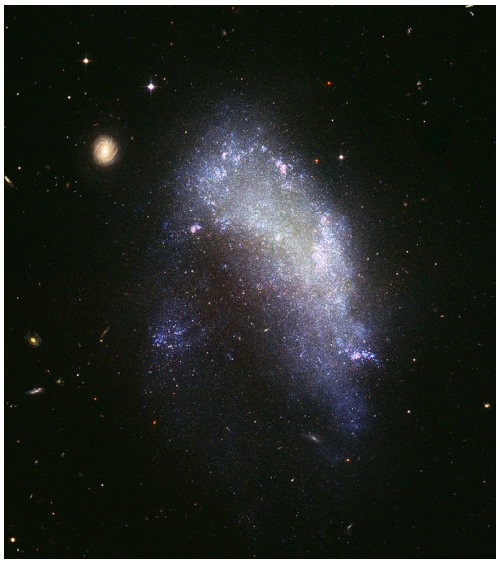

Figure 2.4: An example of an irregular galaxy (NGC 1427A). Image from Wikipedia (2015e), credit AURA, STScI, HST & ESA, NASA.

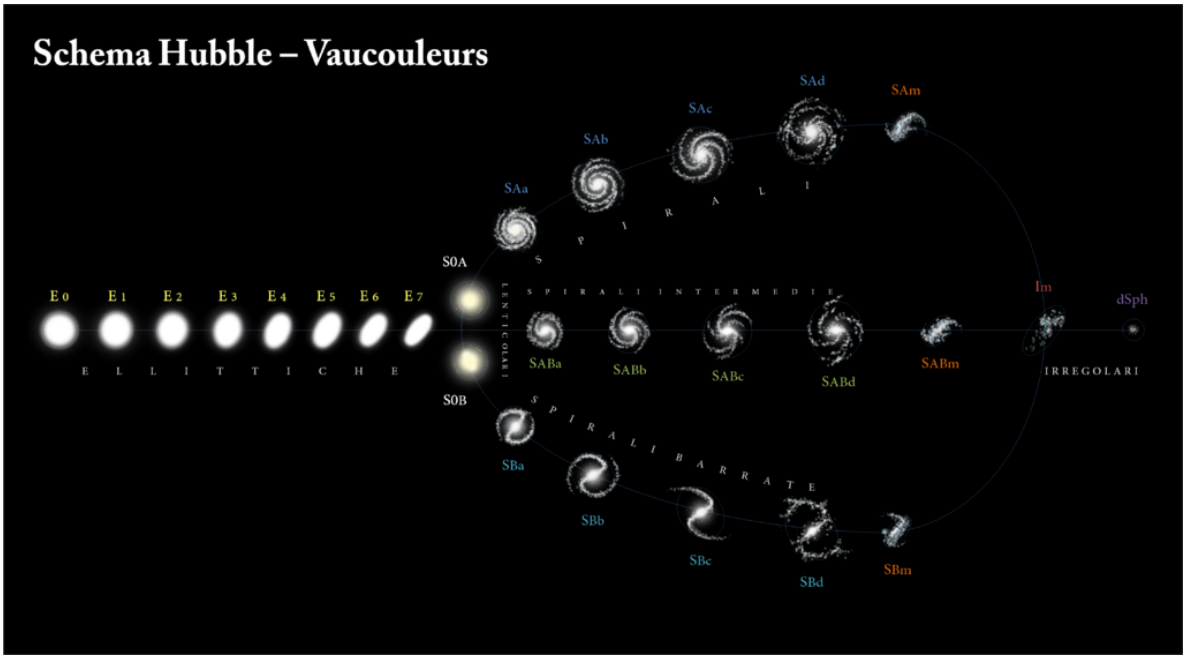

Figure 2.5: The de Vaucouleurs-modified tuning fork, with the addition of intermediate categories between non-barred and barred. Image from Wikipedia (2015c), credit Antonio Ciccolella.

largely due to the limitations of currently available observational data. So it is perhaps not surprising that the process(es) of how exactly spiral structure forms is (are) still up for debate.

Spiral-armed galaxies demonstrate a seemingly paradoxical situation. Since the orbital velocity of matter at all radii is roughly the same, stars closer to the center of the galaxy have higher angular velocities, causing them to "lap" those further out. Without other mechanisms in place, any feature in the disk would get drawn out into a filament that would eventually wind tight, erasing the clearly-defined spiral structure that we see in galactic populations of various ages[1].

Since we see plenty of what appear to be long-lived spirals with open structure, something must be acting against differential rotation. Additionally, the arms contain many O- and B-type stars, and these last only a few Myr (Smith, 1987), much less than the average age of a galaxy in the local universe (about 7-8 Gyr, Gallazzi et al. (2005)). So, there must be something continuously triggering star formation in these regions. The theoretical

[1]See Animation 2 in Wikipedia (2015b) (or `https://upload.wikimedia.org/wikipedia/commons/9/90/Galaxy_rotation_wind.ogv`) for a video example of a galaxy with arms that tighten over time.

formulation that explains these observations must also contend with maintaining a global spiral structure whose size is on the order of tens of kpc.

Lin & Shu (1964, 1966)'s density wave theory is the most influential framework proposed to explain spiral structure. Other theories include development of a swing amplification model (Goldreich & Lynden-Bell, 1965; Toomre, 1981), stochastic star formation (Gerola & Seiden, 1978; Seiden & Gerola, 1979) and manifolds (Athanassoula et al., 2009b,a, 2010), and even a hybrid of swing amplification with transient density waves (Sellwood & Carlberg, 1984; Sellwood, 2011; Sellwood & Carlberg, 2014).

Lin & Shu (1964) first put forth the idea that spiral arms are caused by quasi-stable density waves propagating throughout the disk. Small, non-axisymmetric perturbations cause mass over-densities to amplify to the point allowed by the velocity dispersion of stars and gas (high dispersion tends to smooth out "bumps" in mass distribution). The gravitational field associated with these over-densities causes mass to oscillate radially as it rotates (Lin & Shu, 1967). Combining this with differential rotation, a spiral density wave emerges from overlapping orbits (See Figure 2.6). Spirals are essentially standing waves with boundaries at the middle and at the edge of the galaxy. As the wave moves through the disk, it causes nebulous material to collapse, triggering star formation. Arms are not made up of the same material throughout their entire lifetime. Instead, as stars, gas and dust orbit the center of the galaxy, they move through the waves[2].

The quasi-static density wave theory works well for grand design and other spiral galaxies with continuous arm structure. However, it has been argued that flocculent galaxies, with their feathery, fragmented spirals (Figure 2.7), are better explained by stochastic star formation (Smith, 1987).

Spiral structure formed via stochastic, self-propagating star formation (SSPSF) is the result of combining high-mass stellar dynamics with differential rotation of the disk (Gerola & Seiden, 1978; Seiden & Gerola, 1979). When very large stars approach the end of their lifetime, they may go supernova, sending shock waves through surrounding gas and causing it to expand at high velocities. Adjacent gas clouds will collapse, triggering the formation of new stars. The process then repeats, creating a feedback loop of star formation. Since material that is within these regions but closer to the center of the galaxy orbits with a

[2]See Animation 3 in Wikipedia (2015b) (or `https://upload.wikimedia.org/wikipedia/commons/b/ba/Galaxy_rotation_wave.ogv`) for a video example of a density wave. Note how the stars move through the wave from the latter's frame of reference.

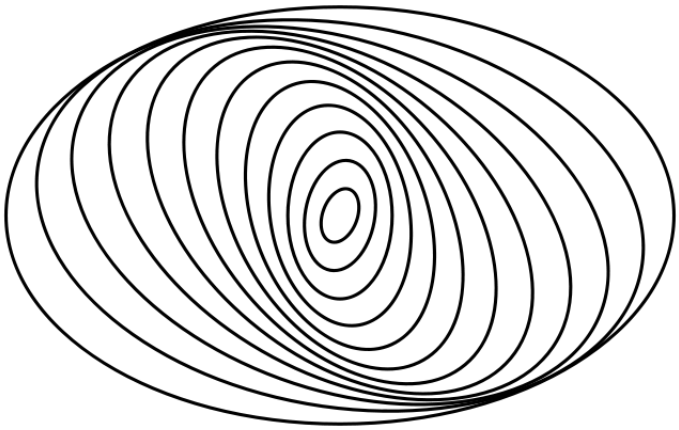

Figure 2.6: Overlapping orbital paths in a galaxy due to density waves. This particular configuration would give rise to two-armed spiral structure. Image from Wikipedia (2015b).

Figure 2.7: An example of a multi-armed, flocculent spiral galaxy. Image from Wikipedia (2014a).

larger angular velocity than material at larger radii, stars and gas are drawn out into a filamentary, spiral shape (see Figure 2.8). Resulting spiral arms are trailing, meaning that stars at the tips "trail" behind those with smaller radii. This large-scale spiral structure rotates "quasi-rigidly" and lasts roughly the lifetime of the galaxy. Since the exact type is determined early on by the rotation curve of the disk, the evolution of a single galaxy from one morphological type to another is limited.

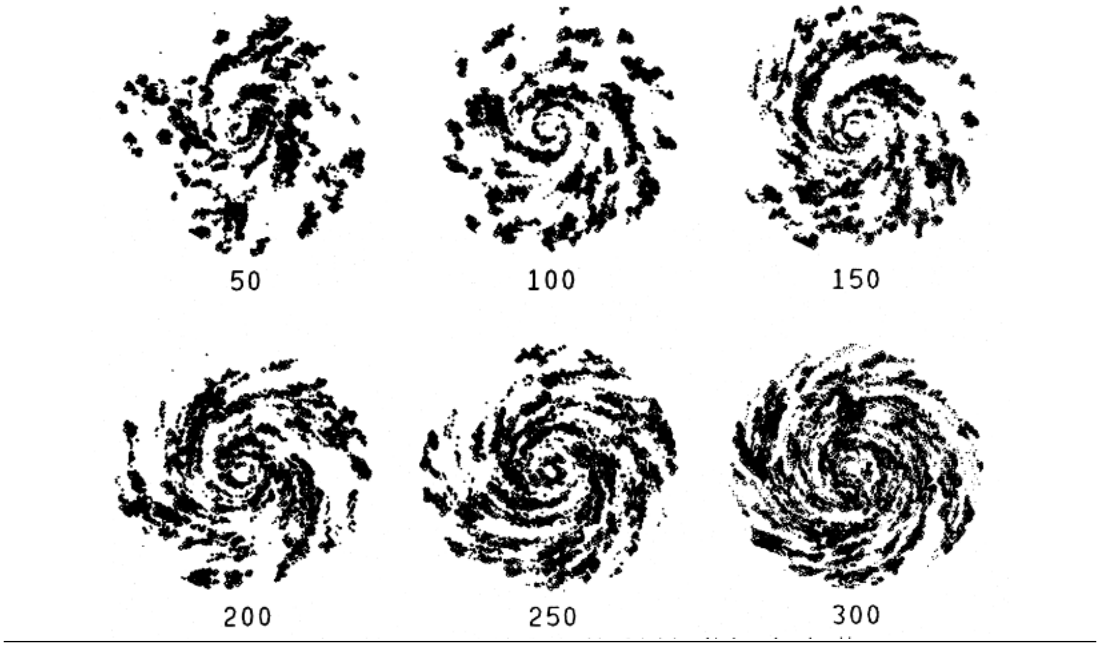

Figure 2.8: Evolution of a model flocculent spiral galaxy formed via stochastic, self-propagating star formation (SSPSF). The numbers represent timesteps, with one timestep being equal to 15 Myr. Pattern rotation is counter-clockwise. Figure 1 from Seiden & Gerola (1979).

It's important to note here that the density wave theory relies on the disk's gravitational potential to trigger stellar formation in specific locations while the SSPSF theory does not, by design, predict the exact location of new stars—initial star formation is random. The manifold theory, however, says nothing about the formation of new stars but does formulate a mechanism that is dependent on the gravitational field of the disk.

The manifold theory has been most successfully applied to barred galaxies exhibiting rings or two-armed spiral structure (Athanassoula et al., 2009b,a, 2010). This theory is based on unstable Langrangian points near the ends of bars (see Figure 2.9), which funnel matter in chaotic orbits into narrow bundles or tubes called manifolds. Particles must be within specific energy ranges to fall into the manifolds. If they are, their ultimate fate depends on

the shape of their manifold, which is governed by bar strength. Stronger bars form spiral manifolds, transporting material outward from the center of the galaxy. Weaker bars form tighter spirals or even rings, the latter trapping particles. Note that this is fundamentally different orbital behavior than that of particles moving according to the density wave theory. Wave-driven particles move roughly perpendicular to the spiral arm as they pass through, whereas manifold-driven particles move *within* the arm. Disk rotation curves play a role as well: for a given bar strength, falling curves are most likely to result in spirals.

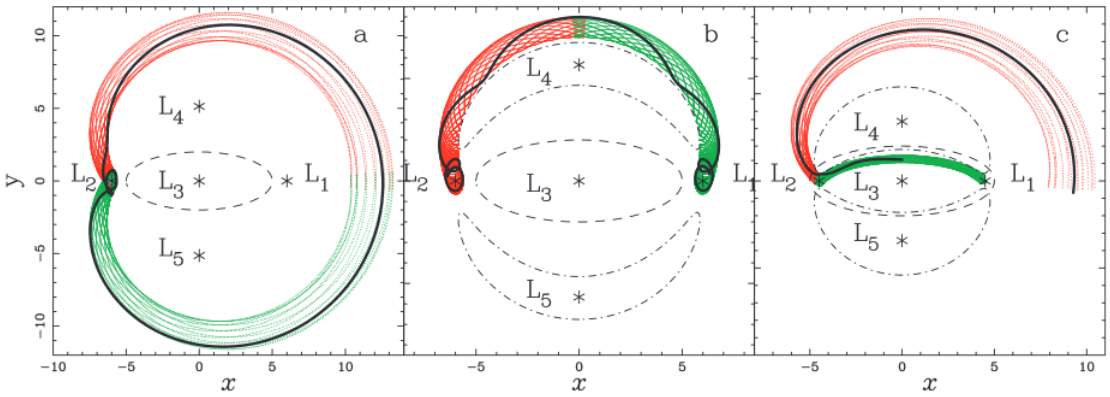

Figure 2.9: Manifolds associated with different types of orbits (left to right, homoclinic, heteroclinic and escaping) and corresponding Lagrangian points. Green indicates the so-called stable manifolds (leading *to* unstable Lagrangian points), red are unstable manifolds (leading *away* from unstable Lagrangian points). Panel (c) shows how material may be funneled from the bar into a spiral arm and to the outer parts of the disk. Figure 1 from Athanassoula et al. (2009a).

Swing amplification theory is, in part, a response to the density wave theory's failure to adequately explain dampening effects (Goldreich & Lynden-Bell, 1965; Toomre, 1981). Density waves should dissipate fairly quickly, making a standing wave pattern impossible. Although density waves are observed in Saturn's rings (which, with Saturn, make up a system like that of a bulge-dominated galaxy), they are associated with forcing mechanisms provided by resonances with Saturn's moons. While outside forces may occasionally generate density waves in galaxies (e.g., when they experience harassment by other galaxies), we see plenty of (relatively) isolated galaxies with spiral patterns. The swing amplification theory posits that differential rotation itself tends to reinforce density waves by swinging them around into trailing arm patterns. In this view, the patterns are likely to be transient rather than long

lasting, but should be common and not dependent on outside forces.

Sellwood & Carlberg's work suggests that spiral arms are driven by the superposition of multiple density waves, with resulting recurrent (neither transient nor long-lived) spiral structure. While the conclusions of this work are grounded mostly in simulation results (with observational data on the longevity of spiral structure inconclusive, see Sellwood (2011) and references therein), they highlight the difficulty of reaching consensus on a theory.

It may be difficult for any single spiral arm formation theories to account for all the morphological features seen in late-type galaxies. The truth may lie in differing mechanisms for different types of galaxies, and perhaps even multiple mechanisms acting in concert in individual galaxies (Athanassoula et al., 2010). There are specific predictions made by each of the theories; both observational and simulation data exists that potentially supports all of these (See Section 2.1.2). For now, we relegate further discussion on data support for the theories to Chapter 5, where we will focus on the results of this study and how they relate to existing theories.

Despite these complications, one thing that most of these schemes have in common is their reliance on the gravitational field in the central part of the galaxy (Berrier et al. (2013), and references therein). This indicates that we must look carefully at indicators of central mass concentration, which we will do in detail in Section 2.2. There, we will also discuss the particulars of density wave theory in regards to mass density.

2.1.2 Pitch Angle

Pitch angle describes the tightness of spiral arms—the tighter the arms, the smaller the pitch angle.

We use the definition of pitch angle in Figure 2.10. To manually measure the pitch angle of a spiral arm, one would first draw a circle centered on the middle of a galaxy's image. At the point where the arm crosses the circle, two straight lines would be drawn—one tangent to the arm and one tangent to the circle. The pitch angle is the angle measured between these two lines.

Pitch angle can vary from $-90°$ to $+90°$. It is positive if the arms wind clockwise and negative if they wind counter-clockwise. More tightly wound spiral arms have pitch angles with smaller absolute values, and looser arms have larger values. As seen in Figure 2.11, when absolute values get closer to zero, spiral arms will more closely resemble a circle.

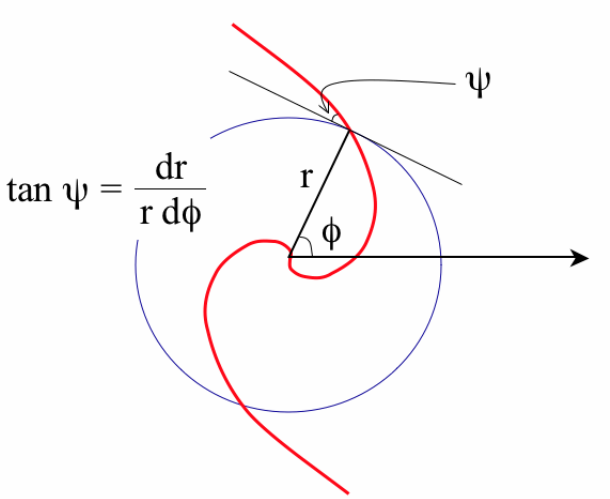

Figure 2.10: The definition of pitch angle, indicated by ψ. Image from Whittle.

Increasingly larger absolute values result in arms straightening out into lines that extend radially from the center of the galaxy.

Since logarithmic spiral arms have the same pitch angle at all radii, one would expect galaxies with logarithmic arm structure to display the same pitch angle at any radius. However, images of real and simulated galaxies show that pitch angle tends to decrease with increasing radius. Other factors affecting measured pitch angle include non-spiral structures such as bars, clumps or spurs. Bars in particular lead to highly-inflated absolute values.

Davis et al. (2012) outline a method to measure the pitch angle of spiral galaxies. Their method uses a 2-dimensional Fast Fourier transform (2DFFT) to decompose images of galaxies into segments of logarithmic spirals, then pieces together pitch angle measurements from those segments.

The method is akin to signal processing. A radial range of the image (in other words, an annulus) is chosen, and 2DFFT attempts to find logarithmic spiral structure within that range, assuming that it will find spirals of a number of arms, m, which are symmetrically placed about the origin (or center of the galaxy and image). An attempt is made to fit $m = 1, 2, .., 6$ arms to the annulus. A pitch angle determination is made based partly on the "signal strength" of the different modes. The one with the strongest signal, or dominant mode, should reflect the number of arms seen in the galaxy image.

Since the choice of inner radius for the annulus greatly affects the pitch angle measurement, Davis et al. chose to anchor the outer radius of the annulus to the visible edge of

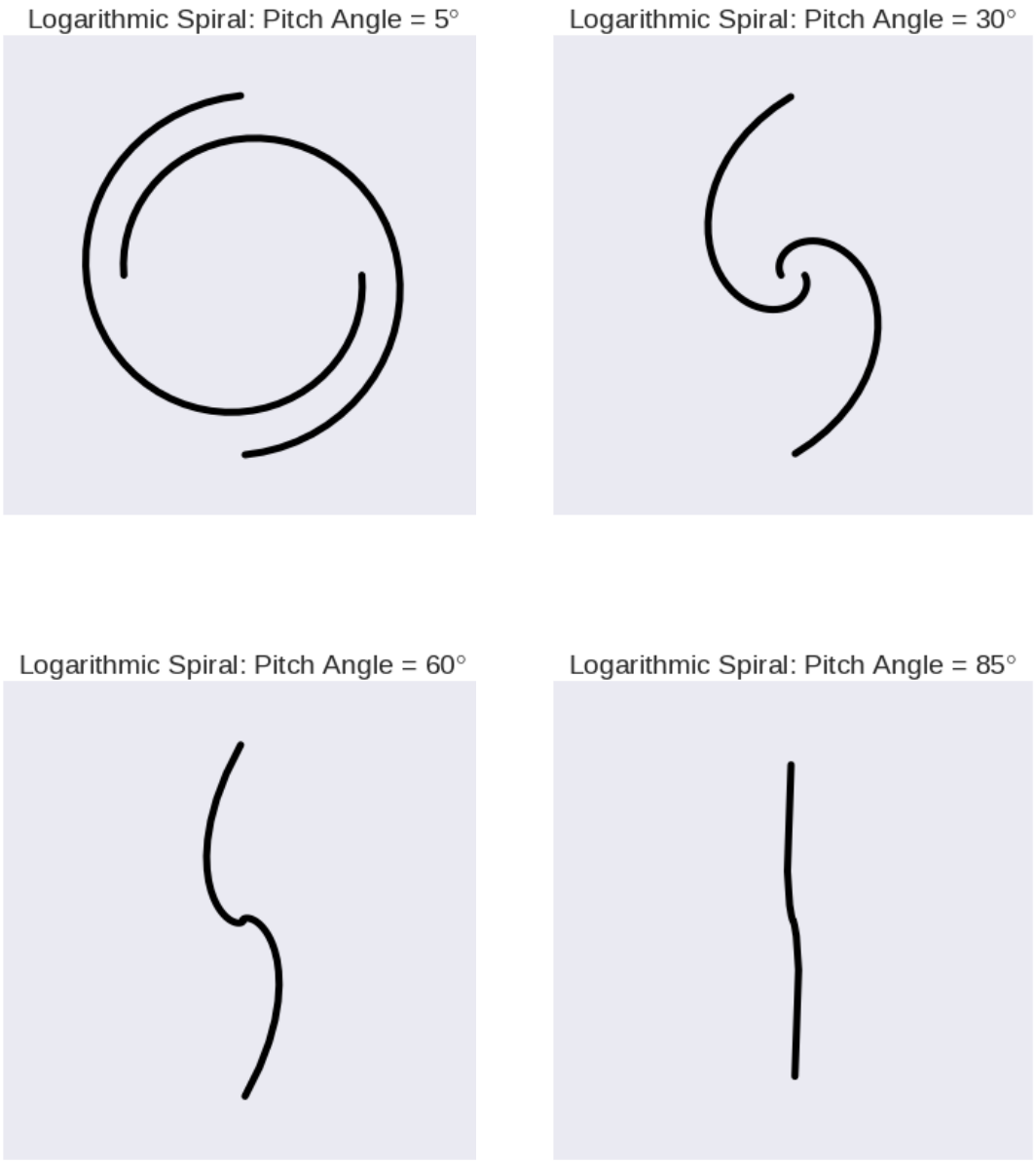

Figure 2.11: Two-armed, logarithmic spirals with pitch angles of positive 5°, 3°, 60° and 85°.

the galaxy and iterate through all possible inner radii. This gives a pitch angle measurement for every annulus, leading to data such as that in Figure 2.12, where one must then choose a radial range where pitch angle is stable, taking the mean as the value.

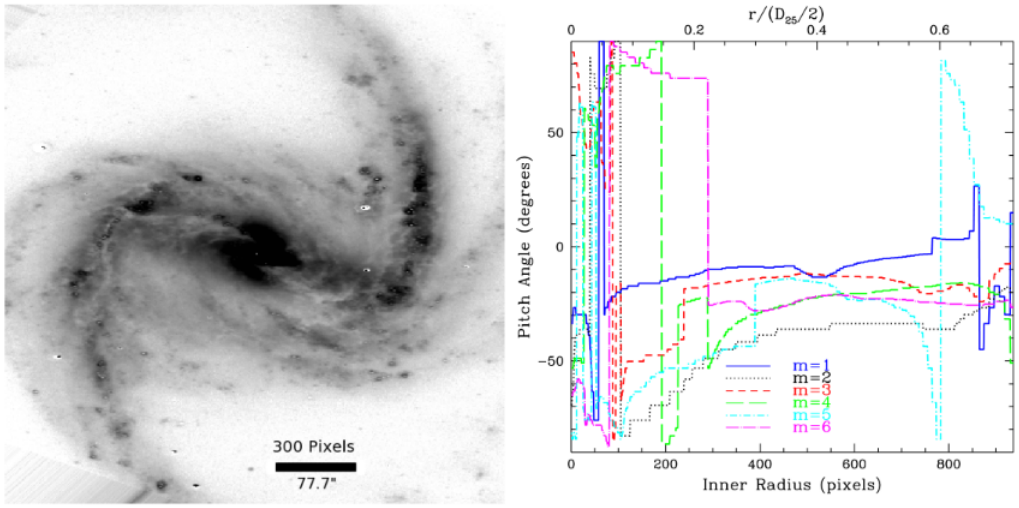

Figure 2.12: An example of pitch angle vs radius data (right) from running 2DFFT on an image of a galaxy (left). Figure 12 from Davis et al. (2012).

Predictions from Theory

The various spiral formation theories make different predictions about the type of structure we might see in disk. Some forecast looser or tighter spirals in certain situations and differing longevity of spiral patterns. Therefore, in theory, we can use pitch angle to distinguish between these frameworks. Although not a main focus of this work, we find it useful to detail these predictions here as a basis for the discussion of our results in Section 5.1, in particular the question of longevity.

The modal density wave theory, with its standing wave patterns, demands that the shape of the resulting spiral be determined by the characteristics of the galaxy. Therefore the pitch angle of the spiral arms should be unchanging over time and should correlate to the host galaxy's bulge mass and disk density.

SSPSF (stochastic, self-propagating star formation) calls for quasi-stable spiral structure long as there is material to replenish star formation (as well as sufficient differential rotation of the disk).

The longevity of spiral arms in the manifold theory depends on sufficient material to populate the arms as well, since bars generally get longer and stronger with time, pushing the Lagrangian points outward. As long as the radial migration of material along the bars does not out pace the growth of the arms, spiral patterns will last indefinitely.

In the swing amplification theory, pitch angle (or tightness) of the spiral arms may change over time, especially as new patterns emerge when older ones disappear.

A recurrent picture, which takes aspects of both density wave and swing amplification theory, expects spiral structure to re-emerge, which will lead to periodic variation in pitch angle.

2.2 Mass Concentration

A relationship between galactic central mass concentration and spiral arm structure is not necessarily unexpected. The Hubble Sequence, seen in Figures 2.3 and 2.5, shows that morphological types with larger bulges tend to have tighter spirals, and those with smaller bulges are inclined towards open arm structure. In other words, increasing the central mass concentration of a galaxy seems to result in a smaller pitch angle.

However, since spiral arms are not explained solely by differential rotation, the actual relationship between central mass concentration and pitch angle is not simple. The gravitational potential of a galaxy's central region does not come from just the roughly spheroidal bulge, but in the case of weakly- or strongly-barred galaxies, also from non-spherical bar features. The dark matter halo affects the orbital velocities of the visible matter in a galaxy, but it is often difficult to separate the halo's contribution to the rotation curve from that of the bulge and disk. The self-gravity of the disk components (namely stars and gas) must also be included in any spiral formation theory.

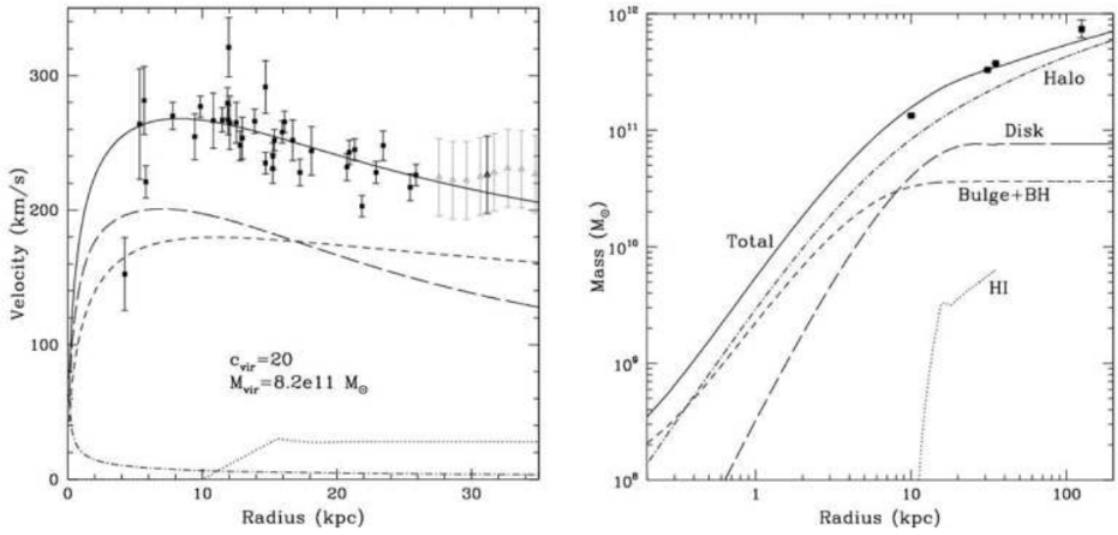

Figure 2.13: An example of rotation curve data (left) and subsequent decomposition into various components by mass (right). Figure 13 from Seigar & Berrier (2011).

There is also the matter of the ubiquitous SMBH (super-massive black hole) at the center of most galaxies. Although SMBH's have a limited region of influence (the inner 1 kpc or so, they are tied to the global spiral structure by way of the $M_{BH} - P$ (black hole

mass and pitch angle) relation (Seigar et al., 2008; Berrier et al., 2013; Davis et al., 2014, 2015). The more massive the black hole, the tighter the spiral arms, and vice-versa.

There are two main reasons to expect this particular relationship from existing observational data: (1) black hole mass is directly related to the gravitational potential at the center of the galaxy and (2) pitch angle has been shown to correlate to quantities that measure gravitational potential. Note that, as mentioned in Section 2.1.1, most theories of spiral arm formation depend on the strength of the gravitational field at the center of the galaxy.

2.2.1 Black Holes and Central Mass Concentration

It is well-accepted that virtually all disk galaxies contain SMBH's at their centers. Measurements of SMBH masses, or M_{BH}, are made through a variety of techniques, most of which estimate the speed of host galaxy material in the relative vicinity of the black hole region. In other words, they probe the gravitational potential well of the black hole. Techniques include reverberation mapping, maser modeling, the Eddington limit, star and gas dynamics, and other relations (Berrier et al., 2013).

The ability to quantitatively describe the bulge as well led to the establishment of correlations between M_{BH} and central mass concentration. These include relations to the velocity dispersion of stars in the bulge (σ; Kormendy & Richstone, 1995; Gebhardt et al., 2000; Merritt & Ferrarese, 2001; Tremaine et al., 2002, bulge luminosity (L_{bulge}; Marconi & Hunt, 2003; Gültekin et al., 2009; McConnell & Ma, 2013), and bulge mass (M_{bulge}; see L_{bulge} references).

In all of these relations, a larger M_{BH} corresponds to a larger number in the other variable as well—in other words, more massive black holes and stronger, gravitational potentials in the central region tend to appear to be correlated, resulting in higher bulge luminosities and masses. However, since black holes are also found in bulge-less galaxies (in the classical sense or otherwise), Seigar et al. (2008), Berrier et al. (2013) and others claim that bulge mass cannot be the sole factor that influences how black holes form and acquire mass. The virial concentration of the dark matter halo has been flagged as one of these possible, additional factors (for more information, see Section 2.2.3).

The sum total of these relationships with M_{BH} led to the expectation and discovery of two correlations: the black hole mass and pitch angle relation ($M_{BH} - P$; Seigar et al.,

2008; Berrier et al., 2013; Davis et al., 2012, 2014, 2015) and the fundamental plane of spiral structure, (Davis et al., 2015).

As predicted by various spiral structure formation theories (including modal density wave theory, see Section 2.1.1), larger black hole masses correlate to tighter spirals. Berrier et al.'s $M_{BH} - P$ relation (given in Figure 2.14) has comparable scatter to the $M_{BH} - \sigma$ relation, and less scatter than the related $M_{BH} - n$ (black hole mass-Sérsic index) relation.

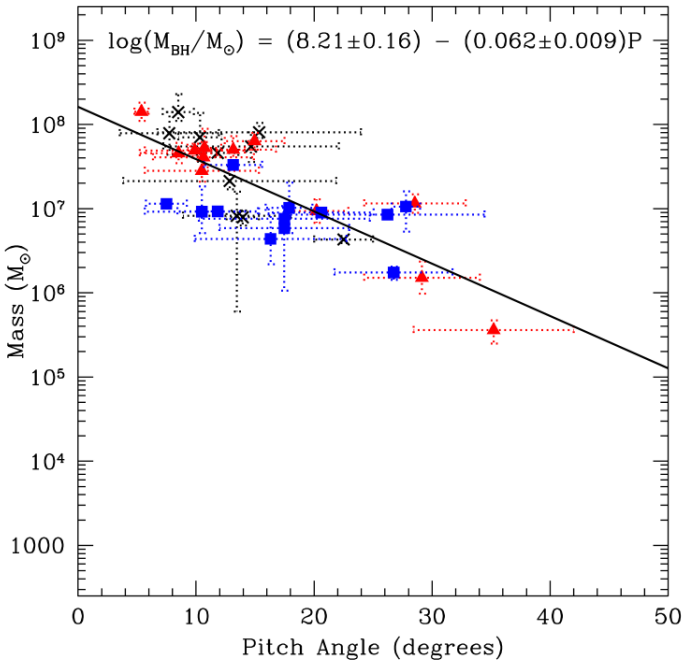

Figure 2.14: The $M_{BH} - P$ relation, showing that larger black hole mass is tied to tighter spiral arm structure in the host galaxy, and therefore smaller pitch angle. The black line shows the best fit, with equation at the top. The marker colors and shapes indicate the different techniques by which black hole masses were obtained. Figure 1 from Berrier et al. (2013).

2.2.2 Pitch Angle and Central Mass Concentration

Davis et al.'s (2014) fundamental plane simultaneously links two parameters to pitch angle, namely central stellar bulge mass and the density of neutral, atomic hydrogen gas in the disk. As seen in Figure 2.15, tighter spiral arms (or smaller pitch angle) indicate larger stellar mass in the bulge, as well as a higher density in the gas component of the disk. This is a relation that is expected from density wave theory.

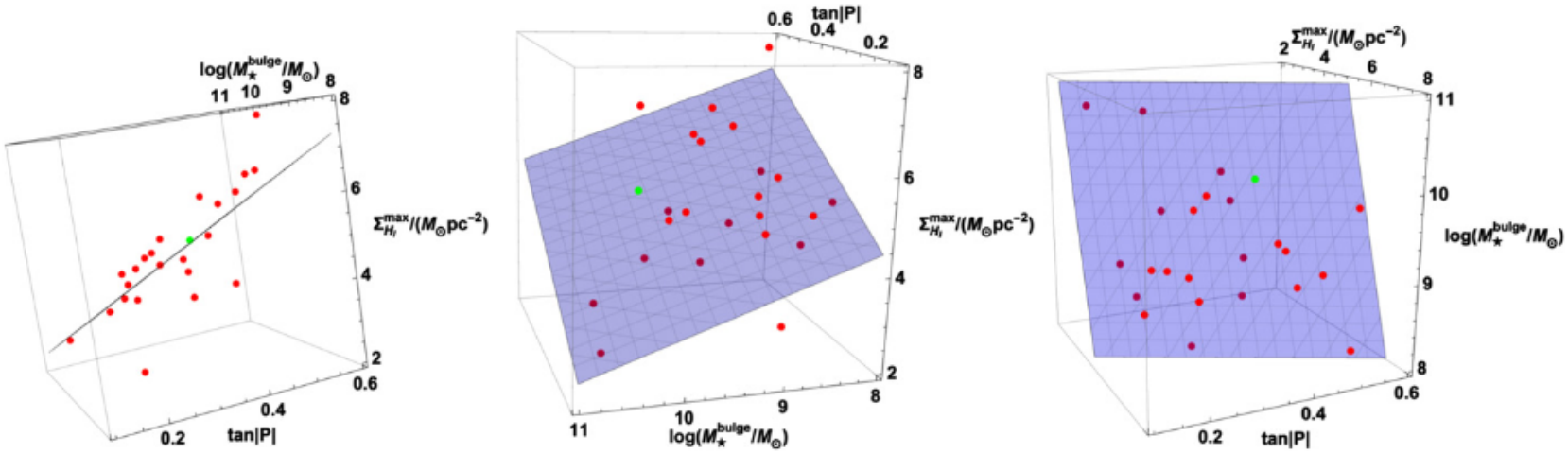

Figure 2.15: The fundamental plane of spiral structure, showing that larger stellar bulge mass is tied to tighter spiral arm structure and higher density of atomic neutral hydrogen in the disk. Figure 2 from Davis et al. (2015).

To augment the discussion on density waves started in Section 2.1.1 as pertains to central mass concentration, we can draw an analogy to standing waves on a string, whose speed of propagation depends on both the density and tension of the string. In a galaxy, the density of the material and the gravitational field of the central region play these parts (Berrier et al., 2013). Bulge-dominated galaxies have pitch angles that are inversely-proportional to the local radial wavenumber (which is dependent on the density and tension mentioned above). It can be shown that for orbits in an equatorial plane of an axisymmetric potential,

$$tan(P) \propto \frac{\sigma_o}{M} \tag{2.1}$$

Where P is the absolute value of pitch angle, σ_o is disk surface density, and M is mass enclosed within the orbital radius (close to M_{bulge}) (Berrier et al., 2013).

Furthermore, it can be shown that for a disk with both stellar and gas components,

$$tan(P) \propto \frac{\sigma_o + F\sigma_*}{M_{bulge}} \tag{2.2}$$

Where P and M_{bulge} are as in Equation 2.1, σ_o is the density of gas in the disk, σ_* is the density of stars in the disk, and $F << 1$ (making gas the primary density factor) (Davis et al., 2015).

Pitch angle has been shown to correlate with other indicators of mass concentration, notably SMBH mass (M_{BH}, as mentioned above, in Section 2.2.1) and shear rate, or S, with high shear rate corresponding to small pitch angle. Support for the $S - P$ relation comes from both observational (Seigar et al., 2005, 2006; Seigar, 2005) and numerical simulation data (Grand et al., 2012b,a, 2013; Michikoshi & Kokubo, 2014).

Shear relates to differential rotation—as particles at different radii (and with different angular velocities) rotate about the center, they may cause breaks in the larger structure as a whole. The relation of shear rates to pitch angle can be partially explained via a modified version of Jean's Theorem (Seigar, 2005). In spherical systems, the balance of velocity dispersion (which is dominant at small scales) and gravity (which is dominant at large scales) is broken at radii above the Jean's length. At these larger distances, over-densities and perturbations will cause gravitational collapse, which can trigger star formation. In flat, disk-like systems (such as spiral galaxies), there will be a region above the Jean length-proper where differential rotation prevents gravitational collapse via shear. The faster the rotation,

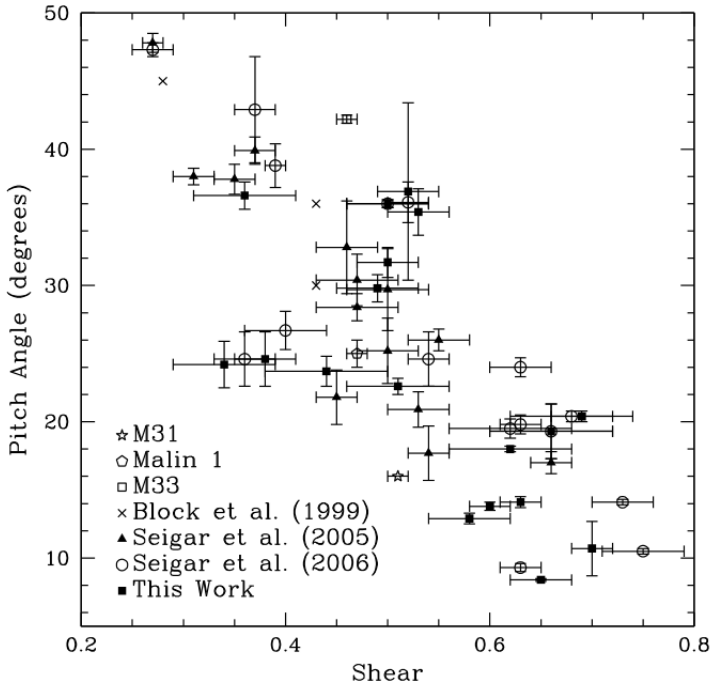

Figure 2.16: Shear rate vs. pitch angle for observational data, featuring measurements from various works, including Seigar et al. (2005, 2006, 2014). Spiral arms tighten with increasing shear rate. Figure 1 from Seigar et al. (2014).

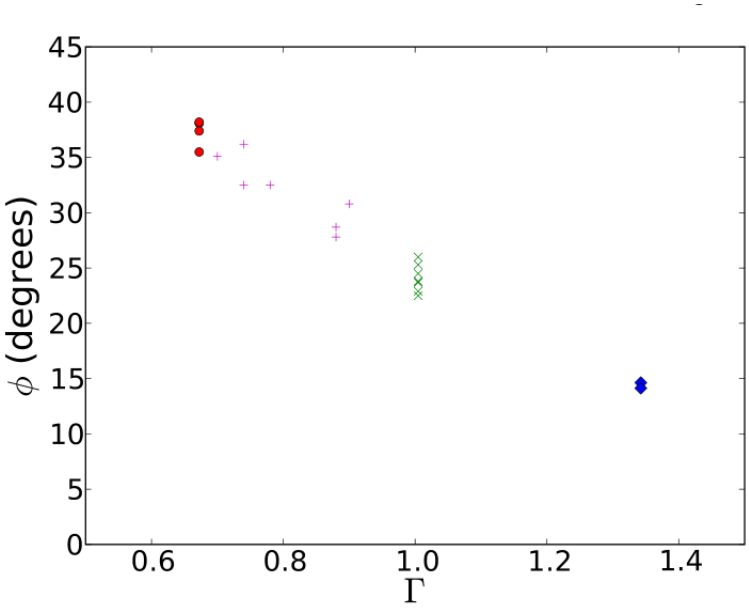

Figure 2.17: Shear rate vs. pitch angle (Γ vs. ϕ) for simulation data from Grand et al. (2013) (Figure 15). Spiral arms tighten with increasing shear rate. Varying markers and colors indicate different models.

the higher the average angular velocity, which is directly proportional to shear rate:

$$S \equiv \frac{A}{\omega} = \frac{1}{2}\left[1 - \frac{R}{V}\frac{dV}{dR}\right] \tag{2.3}$$

Where A is the first Oort constant, ω is angular velocity, V is line-of-sight velocity at radius, R (Seigar, 2005).

Since differential rotation is dependent on the gravitational potential of the central mass, higher shear rates should correspond to steeper potentials, or to higher concentrations of central mass. Some parameters that indirectly measure this concentration do indeed support this supposition. For example, Seigar (2005) has shown that the ratio of far-infrared to K-band luminosities is proportional to shear, and that smaller pitch angles (corresponding to higher central mass) show a rough trend with falling rotation curves and vice-versa. Seigar et al. (2006, 2014) have shown that it is possible, using shear rates inferred from pitch angle, to derive theoretical velocity curves which match observational data for some galaxies, as well as to constrain the dark matter halo density profile.

In 2006, Seigar et al. showed from their models that one should expect virial concentration of the dark matter halo (c_{vir}) and other central mass concentrations to correlate

positively with increasing shear rates, and made the prediction that, given the existing $S-P$ relation, one should therefore see decreasing pitch angle with increasing virial concentration. In 2014, they followed through with observational data from 16 galaxies which shows a weak trend between P and c_{vir} (see Figure 2.18). This suggests and would be further strengthened by a connection between black hole and dark matter halo evolution, but the evidence is inconclusive at best and doesn't support this assertion at worst. Part of the problem is the difficulty is in decomposing the rotation curves of visible matter in observed galaxies to obtain that of the halo.

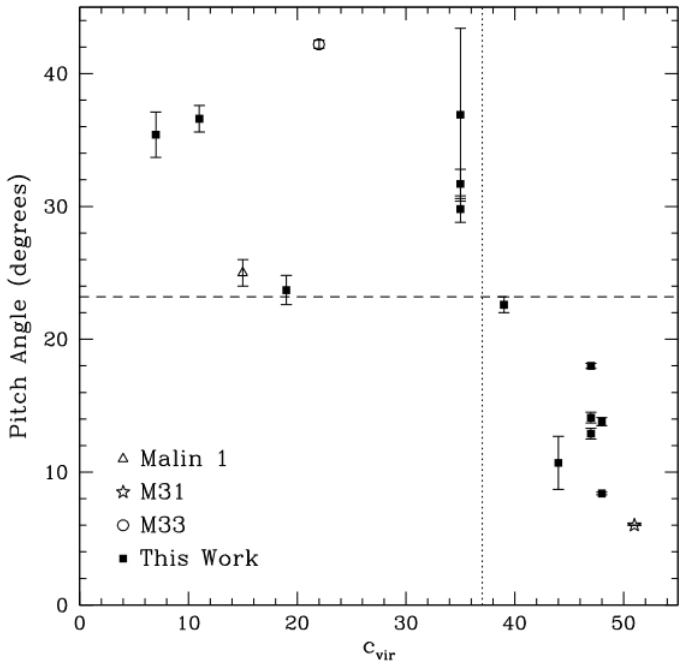

Figure 2.18: A possible trend between c_{vir} vs. pitch angle, showing that tighter spiral arms may correspond to higher density in the core of the dark matter halo. The trend is weak since the sample is small and many of the galaxies with pitch angles $\leq 23°$ have unrealistically high concentrations. Figure 6 from Seigar et al. (2014).

One way to augment the lack of data would be to directly test this assertion via N-body simulations of galaxies, since virial concentration can be directly set or measured. This is the aim of our work here. We provide more details on the particulars of dark matter halos in the next section.

2.2.3 Dark Matter Halos

Since all galaxies are thought to have a halo component, dark matter ties the evolution of individual galaxies to the large scale structure and cosmology of the universe. Hierarchical clustering (which states that amplified density perturbations and gravitational collapse on local scales lead to small structures that merge to create larger forms at later epochs) is the foundation for modern halo formation theory. Navarro et al. (1997) find that the density of halos at their birth (defined as the time at which their constituent parts collapsed) is related to the density of the universe at that epoch. This in turn strongly affects the resulting halo mass at equilibrium.

Halo mass distribution in galaxies is usually modeled according to the so-called NFW profile. This mass density profile is described in a series of papers by Navarro et al. (1995; 1996; 1997). They ran N-body simulations of dark matter halos using a smoothed-particle hydrodynamics (SPH) code. Navarro et al. found that a universal density profile can be used to quantify halos of extensive mass and size ranges, all the way from dwarf galaxy halos to those of galaxy clusters. The NFW profile is given by Equation 2.4 below:

$$\rho(r) = \frac{\rho_{crit}\delta_c}{(r/r_s)(1+r/r_s)^2} \tag{2.4}$$

where,

$$\rho_{crit} = \frac{3H^2}{8\pi G} \tag{2.5}$$

and

$$\delta_c = \frac{200}{3}\frac{c^3}{ln(1+c) - (c/1+c)} \tag{2.6}$$

The critical density of the universe, ρ_{crit}, is dependent on both H, the Hubble constant (which indicates the expansion rate of the universe) and G, the gravitational constant. The characteristic density of the halo, δ_c is a function of c, the concentration. The characteristic radius of the halo is given by $r_s = r_{200}/c$, where r_{200} indicates the radius inside which the mean density is 200 times the critical density.

$$r_{200} = \sqrt[3]{\frac{3}{4\pi}\frac{M_{200}}{200\rho_{crit}}} \tag{2.7}$$

M_{200} is the halo mass interior to r_{200}; these two are sometimes used as proxies for virial mass and radius.

Despite it's great success in adhering to cosmological theory, the NFW profile comes with a few caveats. The first problem is in the profile's behavior at small r. It is too steep, or "cuspy", at the center to describe the halos of some observed populations, including dwarf galaxies. Navarro et al. also report that, in their simulations, NFW halos are also very efficient at drawing baryons (or visible matter) to the center of the halo potential well, compacting the resulting disk component to a size that is smaller than that observed in disk galaxies.

As to the question of interaction between the dark matter halo and the disk, and in particular how this affects the spiral structure according to the density wave or manifold theory, etc., we need look at which halo parameters contribute directly to variables known to correlate with pitch angle. We already have some evidence that c_{vir} (c in the NFW profile) may be correlated to pitch angle (see above section, 2.2.2).

However, Navarro et al. suggest that, without additional mechanisms in place (such as supernova feedback and stellar winds) in numerical simulations of galaxies, predictions about the NFW halo/disk interaction are somewhat ambiguous. For instance, to match observed rotation curves for disk galaxies (including those that are spiral-armed), it is necessary to adopt a ratio of disk mass to disk luminosity that is not constant, but increases with luminosity. So, there is the possibility that the halos of more luminous galaxies do not contribute to disk velocities in the same way that halos of less luminous galaxies do—this is not a trivial matter since luminosity is an indicator of disk and bulge mass.

Seigar et al. (2006) indicate that the relative speed at which baryons fall into the halo's potential well can be made slower by adiabatic contraction of the halo over the galaxy's evolution. This would produce disks that better align with observations, but also results in larger halo virial concentrations. However, not all galaxies appear to be well-described by adiabatically-contracted halos with large virial concentrations. This is a problem when interpreting a possible $c_{vir} - P$ relation.

Other parameters known to correlate with pitch angle have an unclear relationship with dark matter halos. Treuthardt et al. (2012) cite arguments both for and against an $M_{BH} - c_{vir}$ relation. Using bar speed as a proxy for halo concentration and pitch angle as a proxy for black hole mass, they could find no correlation. Specifically, they found that galaxies with low dark matter concentrations had a wide range of black hole mass.

At the present, it seems unclear how exactly one would interpret a $c_{vir} - P$ relation from N-body simulations (or a lack of one) without having additional measurements pertaining to known halo concentration or pitch angle relations and without quantifying the effects of processes left out of those simulations (such as supernova feedback).

3 Methods

In order to test the question of whether or not virial concentration (c_{vir}) is correlated with pitch angle (P), we ran N-body simmulations of 11 isolated, barred spiral galaxies for 3 Gyr. These models differ mainly in the virial concentration of their initial conditions, with slight differences in particle mass. We then simulated observational images from the N-body output and measured their pitch angle over time at regular intervals.

In this chapter, we detail the various steps needed to run the simulations, including descriptions of the various pieces of software necessary and the data pipeline. We also describe our method for measuring pitch angle, which is an updated version of Davis et al.'s (2012).

In Section 3.1, we outline the model and parameters used to set up the initial conditions of the model galaxies. We describe the software and parameters used to evolve the models in Section 3.2. Section 3.3 details our pitch angle measurement process.

3.1 Initial Condition Set-Up

The first part of running a successful N-body simulation is building the initial conditions, which are then fed into the software that evolves the system according to a particular physical framework.

3.1.1 Model Galaxy Template

The initial conditions for our simulations were made with the use of GalactICS, a model of late-type galaxies based on the Milky Way (described in Widrow et al. 2008). The axisymmetric model has three components—a Sérsic bulge, an exponential disk and a cuspy dark matter halo. The bulge and disk particles represent the mass of stars (or visible matter), whereas the halo particles represent the mass that extends past the visible portion of a galaxy. The model can, in principle, contain gas particles as well, but we omitted these for the sake of simplicity.

GalactICS was chosen for the ability to change parameters associated with mass concentration in the dark matter halo, as well as the ability to convert initial condition files

into a format compatible with the chosen simulation software, Gadget-2 (see Section 3.2), and output files into the FITS format necessary for the pitch angle measurement process.

Most models of galaxy structure are based on solutions to the collisionless Boltzmann and Poisson equations for a system initially in equilibrium (Heggie & Hut, 2003). These models begin with the assumption that the mass of a galaxy can be described by a distribution function which resides in a 6-dimensional phase space (three position plus three velocity or momentum coordinates. Such a function gives the probability that a parcel of mass with position vector r and velocity v (or momentum p) resides in a given volume within the phase space. In order to describe a multi-component structure (e.g., a galaxy with a bulge, disk and halo), the function must have a corresponding term for each component. Widrow et al. (2008) construct a distribution function of the form,

$$f(\mathcal{E}, L_z, E_z) = f_d(\mathcal{E}, L_z, E_z) + f_b(\mathcal{E}) + f_h(\mathcal{E}) \tag{3.1}$$

Where the subscripts indicate the disk, bulge and halo components respectively. $\mathcal{E} = -E$ is the relative energy, L_z is the angular momentum about the symmetry axis and E_z is the energy of stellar vertical motion in the disk. Integrating Equation 3.1 over all velocities gives a density profile of the form,

$$\rho(R, z, \Psi) = \rho_d(R, z, \Psi) + \rho_b(\Psi) + \rho_h(\Psi) \tag{3.2}$$

Where R and z are the cylindrical coordinates, $\Psi = -\Phi$ is the relative potential (Φ being the gravitational potential), and $\rho(R, z, \Psi)$ satisfies Poisson's equation, $\nabla^2\Psi = -4\pi G\rho(R, z, \Psi)$. Widrow et al. (2008) use $G = 1$.

The halo and bulge components start out spherically symmetric, but since the non-spherical disk is added in, the halo and bulge become axisymmetric at equilibrium. So GalactICS's initial conditions are built such that target density profiles, $\tilde{\rho}_i$, are approximated via spherical harmonic expansions.

The target bulge density profile is,

$$\tilde{\rho_b}(r) = \rho_b \left(\frac{r}{R_e}\right)^{-p} e^{-b(r/R_e)^{\frac{1}{n}}} \tag{3.3}$$

Where $p = 1 - \frac{0.6097}{n} + \frac{0.05563}{n^2}$ and n is the Sérsic index. b is adjusted so that R_e is the radius enclosing half of the bulge mass.

The target halo density profile is,

$$\tilde{\rho_h}(r) = \frac{2^{2-\gamma}\sigma_h^2}{4\pi a_h^2} \frac{C(r : r_h, \delta r_h)}{(\frac{r}{a_h})^\gamma (1 + \frac{r}{a_h})^{3-\gamma}} \tag{3.4}$$

Where a_h is the halo scale length, σ_h is the velocity scale, and γ is the steepness of the density profile as $r \to 0$, or the "cuspiness." $C(r : r_h, \delta r_h)$ is a truncation function that goes from $1 \to 0$ at $r = r_h$ over a width δr_h, or

$$C(r : r_h, \delta r_h) = \frac{1}{2} \operatorname{erfc}\left(\frac{r - r_h}{\sqrt{2}\delta r_h}\right) \tag{3.5}$$

Note that the target halo profile, when given a value of $\gamma = 1$, is the same as the NFW halo profile (Equation 2.4), save for some constants and the truncation function.

Widrow et al. (2008) use a modified version of Kuijken & Dubinski's (1995) disk density profile,

$$\tilde{\rho_d}(r, z) = \frac{M_d e^{-r/r_d}}{4\pi r_d^2 z_d} C(r : R_{out}, \delta r_d) \tag{3.6}$$

Where M_d is the total disk mass, r_d is the disk scale length, R_{out} is the outer disk radius, and $C(r : R_{out}, \sigma r_d)$, the disk truncation function, has the same form as the halo truncation function.

The halo density profile has two parameters in particular, γ and a_h, that can be varied to achieve differing c_{vir} values. They are connected through the following relation:

$$c_{vir} = R_{vir}/R_s \tag{3.7}$$

Where R_{vir} is the virial radius and R_s is the radius at which the logarithmic slope of the halo density profile is negative two. For the profile in Equation 3.4, R_s is given by:

$$R_s = (2 - \gamma)a_h \tag{3.8}$$

3.1.2 Models

In order to vary the mass concentration of the dark matter halo component in GalactICS, one can change the "cuspiness" parameter, γ, and/or the scale radius a_h.

To choose values for these two variables, we looked at the parameter space of c_{vir}.

Model	γ	a_h	R_s	Min. c_{vir}	Max. c_{vir}
a1	0.4	5	8	25.0	65.0
a2	0.4	15	24	8.333	21.67
a3	0.4	25	40	5.0	13.0
b1	0.8	4	4.8	41.67	108.3
b2	0.8	15	18	11.11	28.89
b3	0.8	25	30	6.667	17.33
nfw1	1.0	5	5	40.0	104.0
nfw2	1.0	15	15	13.33	34.67
nfw3	1.0	25	25	8.0	20.8
c1	1.2	5	4	50.0	130.0
c2	1.2	15	12	16.67	43.33
c3	1.2	25	20	10.0	26.0

Table 3.1: Parameters of model galaxies. γ and a_h were directly varied in the initial condition generator, while R_s values come from Equation 3.8. Minimum and maximum values for c_{vir} come from an R_{vir} range of 200-520 kpc and Equation 3.7.

According to Widrow et al. (2008)'s models of adiabatically decontracted dark matter halos, c_{vir} and R_{vir} have likely values of 5-50 (dimensionless) and 200-520 kpc, respectively. This gives a range of 4-104 kpc for R_s (see Equation 3.7).

Additionally, Widrow et al. (2008) cite likely values of 0-1.5 (dimensionless) and 0-30 kpc for γ and a_h, respectively. These further restrict R_s to 4-45 kpc (see Equation 3.8 and Figure 3.1).

As can be seen in Figure 3.2, the parameter space of Equation 3.8 shrinks as a_h becomes larger (closer to 30 kpc) and γ becomes smaller (closer to 0). This means that dark matter halos with these parameter values are not likely, so we avoided those extremes. We chose $\gamma = 0.4, 0.8, 1.0, 1.2$ for model categories *a*, *b*, *nfw*, and *c*. By varying a_h within each category, we obtained a total of 12 unique parameter combinations that were then fed into GalactICS (see Table 3.1). All but model *nfw3* resulted in numerically viable initial conditions and were used to evolve isolated spiral galaxies.

Although all 11 models have the same particle numbers (Table 3.3), particle masses were not exactly the same across all models for any component (Table 3.2).

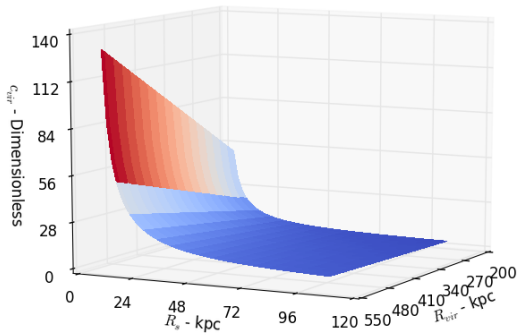

(a) View 1

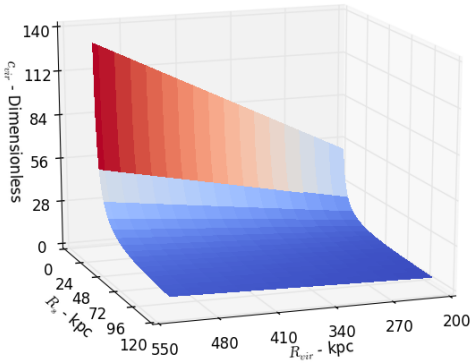

(b) View 2

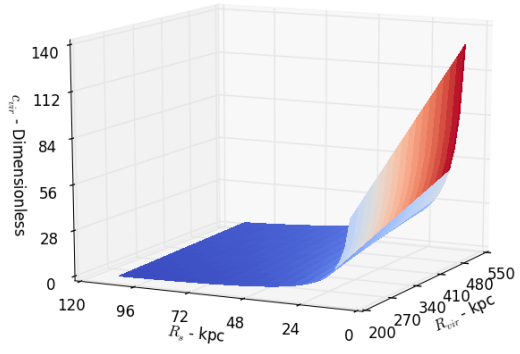

(c) View 3

Figure 3.1: The parameter space of Equation 3.7, or $c_{vir} = R_{vir}/R_s$.

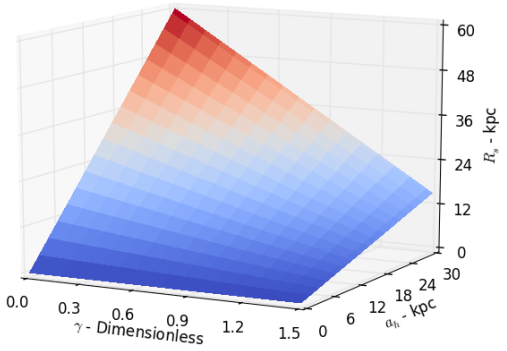

(a) View 1

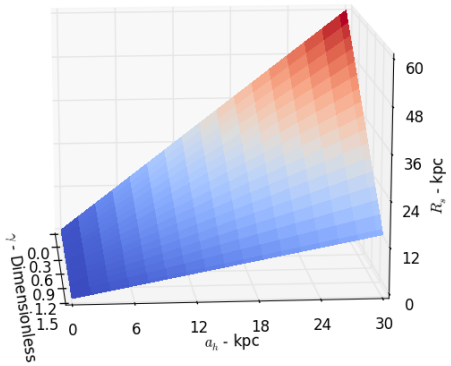

(b) View 2

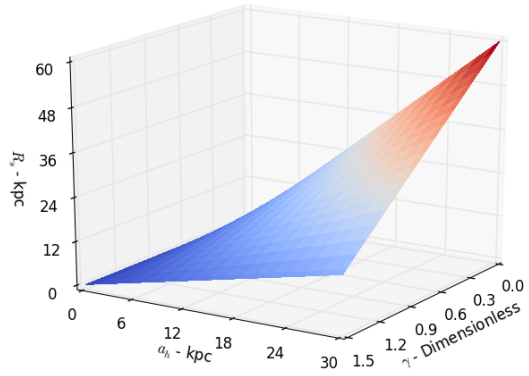

(c) View 3

Figure 3.2: The parameter space of Equation 3.8, or $R_s = (2 - \gamma)a_h$.

Model	m_b	m_d	m_h	M_{tot}
a1	2.9555×10^{-1}	3.1639×10^{-1}	1.9576×10^{-1}	3.5145×10^{6}
a2	2.9883×10^{-1}	3.1289×10^{-1}	3.5817×10^{-1}	5.9166×10^{6}
a3	2.9972×10^{-1}	3.1164×10^{-1}	3.7450×10^{-1}	6.1567×10^{6}
b1	2.9305×10^{-1}	3.1722×10^{-1}	1.6118×10^{-1}	3.0028×10^{6}
b2	2.9723×10^{-1}	3.1416×10^{-1}	3.3167×10^{-1}	5.5255×10^{6}
b3	2.9860×10^{-1}	3.1278×10^{-1}	3.1394×10^{-1}	5.2608×10^{6}
nfw1	2.9143×10^{-1}	3.1772×10^{-1}	1.4669×10^{-1}	2.7885×10^{6}
nfw2	2.9595×10^{-1}	3.1502×10^{-1}	2.5741×10^{-1}	4.4261×10^{6}
nfw3	2.9744×10^{-1}	3.1366×10^{-1}	3.5123×10^{-1}	5.8146×10^{6}
c1	2.8968×10^{-1}	3.1831×10^{-1}	1.8431×10^{-1}	3.3465×10^{6}
c2	2.9390×10^{-1}	3.1613×10^{-1}	2.4452×10^{-1}	4.2364×10^{6}
c3	2.9559×10^{-1}	3.1484×10^{-1}	3.4216×10^{-1}	5.6816×10^{6}

Table 3.2: Model galaxy masses, all in units of $1 \times 10^5\ M_\odot$. m_b, m_d and m_h are the masses of individual bulge, disk and halo particles, respectively. M_{tot} gives the total mass, or $\sum_i m_i N_i$, where $i = b, d, h$ and N_i is the number of particles for a given component.

Component	Type	No. of Particles
Bulge	Stellar	279 595
Disk	Stellar	1 677 721
Halo	Dark Matter	14 819 900
	Total	$256^3 = 16\,777\,216$

Table 3.3: Types and numbers of particles for all models.

3.1.3 Format Conversions

After initial condition files were generated for all 11 models, they had to be converted into a format compatible with the Gadget-2 simulation software (Springel, 2005). As an intermediary between GalactICS and Gadget-2, we used the TIPSY file format[1].

GalactICS outputs many files for every set of initial conditions it creates, including one each for the disk, bulge and halo components. Each component file has mass, position and velocity information for every particle. Other information produced by the initial condition generator (such as energy, angular momentum, etc.) could potentially be used in the simulations, but was left out here since it is common practice to feed only mass, position and velocity (or momentum) data to simulator software.

The first format conversion we did was from GalactICS ASCII (text) to TIPSY ASCII formatting. Then, we converted from TIPSY ASCII to the standard (binary) TIPSY format. Finally, we converted to the Gadget-2 binary format.

[1]TIPSY is a file format that is part of the larger suite of numerical simulation software created by the N-Body Shop at the University of Washington, including ChaNGa (Jetley et al., 2008; Menon et al., 2015).

3.2 Running Simulations

We used the Gadget-2 software (Springel, 2005) to evolve each of our 11 model galaxies in isolation. Gadget-2 is a TreeSPH code: all matter types (stellar, gas and dark matter) are treated as particles, gravitational interactions are computed via a hierarchical tree method that utilizes multipole expansions, and gas interactions with smoothed particle hydrodynamics (SPH)[2].

The physical framework of the simulations can be individualized to a certain extent. For example, one can choose to compute short-range forces directly while approximating long-range forces (e.g., the TreePM algorithm). One can also set values related to the cosmological model of the universe. Some of variables are set in the Makefile used in compiling the program's executable, others are set in the parameter file for individual simulations. We selected the same Makefile and parameter options for all simulations to ensure that the only differences between models were those specified in creating initial conditions (see Section 3.1.2). See Tables 3.4 and 3.5 for Makefile options and parameter values chosen.

Makefile Options
UNEQUALSOFTENINGS
PMGRID = 256
SYNCHRONIZATION

Table 3.4: Some of the Makefile options used to compile the Gadget-2 executable. From top to bottom: *UNEQUALSOFTENINGS* is chosen when all particles are not given the same softening lengths. *PMGRID* enables the TreePM method and indicates the mesh dimensions used to calculate the long-range forces. *SYNCHRONIZATION* is a TreePM-related option.

Softening length, which is akin to a minimum inter-particle distance, is used to avoid unrealistically large forces on the particles (and therefore sudden and large velocity changes) in N-body simulations. Stellar particles are usually given a softening length on the order of 10 pc, and dark matter particles on the order of 1 kpc.

However, because of the large number of particles in our models ($\approx 10\times$ greater than other N-body simulations; see Widrow et al. (2008); Grand et al. (2012a, 2013); Michikoshi & Kokubo (2014)), we found that a more realistic softening length vastly increased the amount

[2]Note that, since we did not introduce gas particles into our models, our simulations did not make use of SPH.

Parameter	Value	Unit
TimeBegin	0.0	Gyr
TimeMax	3.0	Gyr
TimeBetSnapshot	0.05	Gyr
MaxSizeTimestep	0.01	Gyr
MinSizeTimestep	0.0	Gyr
OmegaLambda	0	critical density (at $z = 0$)
UnitMass_in_g	1.9890×10^{33}	($1\ M_\odot$)
SofteningHalo	1.0	kpc
SofteningStars	1.0	kpc
SofteningHaloMaxPhys	1.0	kpc
SofteningStarsMaxPhys	1.0	kpc

Table 3.5: Gadget-2 parameters that were changed from their default values or require specific values for simulations in Newtonian space. Parameter groupings, top to bottom: (1) *TimeBegin*, *TimeMax* and *TimeBetSnapshot* specify the beginning and end of the simulation in internal time, as well as the time between consecutive snapshots. *MaxSizeTimestep* and *MinSizeTimestep* indicate the precision of the time integration. (2) Ω_Λ, the cosmological vacuum energy density, must be zero in Newtonian space. (3) We set *UnitMass_in_g*, the internal mass unit, to approximately 1 $M_\odot$, or 1.9890×10^{30} kg. (4) For consistency, maximum softening length for each type is set equal to the minimum value. Note that, within Gadget-2, bulge and disk particles are classified as "Stars" instead of as types "Bulge" and "Disk".

of computation time necessary to complete an entire simulation. In a series of tests, we saw that for disk softening lengths of 0.01 kpc to 0.15 kpc, an increase in total particle number from 3×10^6 to 3×10^7 resulted in a decrease of simulated time by about a factor of 100. Therefore, we set the softening length of all particles to 1 kpc.

Another aspect of running simulations is in choosing the appropriate number of cores to utilize on a parallel computing system. In general, throwing more and more cores at a computational problem does not decrease the amount of time needed to finish a given number of computations since, past some optimum number of cores, communication between cores and work-load imbalance increases at a rate greater than any additional increase in floating point operations per second. In a second series of tests, we saw that the increase in completed simulation time between 2^6 and 2^7 cores was substantially less than the increase between 2^5 and 2^6 . The same held for the difference between 2^7 and 2^8. Since the best computing platform available to us at the time had nodes with 16 cores each, we settled on 64 cores.

3.3 Pitch Angle Measurement

After evolving our model galaxies, we simulated observational images from our numerical output, then ran this image data through a two-dimensional, fast Fourier transform. Finally, we selected pitch angle measurements from the transform output for as many modes as possible in order to fully describe the evolution of pitch angle.

Our approach differs from that of Davis et al. (2012) in that we automate as much of the process as possible, including systematic pre-selection of pitch angle vs radius stable regions, as well as precise, digital spiral overlays of images to confirm pitch angle measurements.

3.3.1 Simulating Observational Data

Since the method we used to measure pitch angles was developed for observational data (Davis et al., 2012), the numerical simulation output can't be directly used to obtain pitch angles. Instead, we made mock observational images of our model galaxies by converting particle mass and position information from Gadget-2 output files to pixel brightness values in FITS[3] images.

We converted the Gadget-2 snapshots to Tipsy binary format, then transformed that to postscript using an IDL[4] script. Note that any script that mocks observational data (namely luminosity) from particle information makes some assumptions about the mass-to-light ratio. In this case, we assumed a constant ratio over all radii. It is also possible to cut off luminosity below or above certain values. For ease of pitch angle measurement, we simulated images as if seeing the galaxy face-on.

Finally, we can either use a script that calls ImageMagick[5] and Ghostscript[6] functions or use GIMP[7] to do the final conversion to FITS files.

[3]The Flexible Image Transport System, or FITS, is a raster-style format commonly used in astronomy to store both images and image data. See `http://fits.gsfc.nasa.gov/`.
[4]`http://www.exelisvis.com/ProductsServices/IDL.aspx`
[5]`http://www.imagemagick.org/script/index.php`
[6]`http://www.ghostscript.com/`
[7]`http://www.gimp.org/`

3.3.2 Image Preparation for 2DFFT

Prior to measuring pitch angles with 2DFFT, the galaxy image must be modified and converted into a text file for input into 2DFFT.

2DFFT assumes that spirals in the image are "face on" (not inclined) to the viewer, that the image is square, with the center of the spiral at the center, and that there are no other structures present in the image (i.e., other galaxies, stars, etc.).

First, one finds the center of the galaxy in the FITS image, and then the outermost radius. Using the known center and radius, the image is cropped and finally converted into text format.

All these steps can be done "manually" by typing the appropriate IRAF[8] commands and visually inspecting the image. However, due to the nature of N-body simulations, large numbers of images can be produced, especially if dumps are made with a frequency meant to sample at a high temporal resolution, or if multiple simulations are done.

In our case, we had 11 models and 61 snapshots per model, and we also had to consider multiple modes per image, so it was prohibitive to perform all steps by hand. We therefore introduce 2DFFT Utilities[9], an open-source collection of scripts and tools created by the author and used to automate and ease various aspects of the 2DFFT data pipeline.

2DFFT Utilities makes use of Python-based packages such as PyRAF[10], Astropy[11] and other freely-available software tools. 2DFFT Utilities is a work in progress, and in its current iteration, is focused on the automation of pitch angle measurement for N-body simulated galaxies. However, it can be used to measure pitch angles for observational images that are already face-on.

We used 2DFFT Utilites were used to do batch image pre-processing (such as finding the center and cropping[12]), as well as to perform various analysis tasks described in Section 3.3.3.

[8] `http://iraf.noao.edu/`

[9] 2DFFT Utilties and documentation can be found at: `https://github.com/AGES-UARK/2dfft_utils`.

[10] PyRAF is a product of the Space Telescope Science Institute (STScI), which is operated by AURA for NASA; see `http://www.stsci.edu/institute/software_hardware/pyraf`.

[11] See `http://www.astropy.org/`, or the Astropy paper (Astropy Collaboration et al., 2013).

[12] Note that while we manually found the radius for all images used in this work, a script to automatically find radius is in progress. See: `https://github.com/AGES-UARK/2dfft_utils/pull/2`.

3.3.3 Pitch Angles from 2DFFT Output

Once the text files from the FITS images have been run through 2DFFT, one takes the output (pitch angle vs radius and p_{max} vs radius) and plots it (see Section 2.1.2). To make sense of the 2DFFT data, it is necessary to determine which modes dominate a given galaxy–its not always sufficient to base this on visual inspection of the image. Determining pitch angle is not trivial, either. Real and realistically-simulated galaxies are not perfectly logarithmic throughout the disk, so pitch angle changes with radius. Highly-linear features such as the bar also artificially inflate pitch angle measurements at radii associated with those features.

To determine pitch angle for a given image, we adhered to the following guidelines:

1. Confirm dominant mode(s) by visually inspecting the image and p_{max} vs radius data.
2. Find ranges of radius in which pitch angle is relatively stable for each mode of interest.
   (a) Select range outside of bar/bulge/central-most region...
   (b) ...But select range that is otherwise closest to the center.
   (c) Never select pitch angle from the outer 10 % or so radii.
3. Visually confirm pitch angle by overlaying galaxy image with logarithmic spirals.
   (a) The overlay should match the galaxy in the same radial range as chosen.
4. If a reasonable pitch angle cannot be chosen for a particular mode/snapshot/galaxy, don't force a measurement.

Stable region selection for pitch angle vs radius was semi-automated by a script in 2DFFT Utilities (*slope_change.py*) that selects candidate ranges based on sudden changes in slope. The user still has to pick the final range, but the boundaries of the ranges themselves are chosen in a consistent manner that eliminates human error while allowing the user to adjust how stable regions are defined. For example, the user can exclude danger areas that are close to the center and edge (which tend to give artificially high or low pitch angles), minimum region length as a percentage of the outer radius, minimum slope change to mark the range boundaries, etc.

A tool to help with visually confirming pitch angle by digitally over-laying images with spirals is also included in 2DFFT Utilities (*overlay-test_cmap-scales.py*), soon to be replaced by a GUI version[13].

It should be noted that since all of our models developed bars, it was especially important to define the area of interest for both selecting stable regions and for visually confirming pitch angle as being the part of the arms that are close to the ends of the bars (where the arms originate).

Pitch angle error was calculated in a way similar to that of Davis et al. (2012). We used the formula,

$$E_\phi = \sqrt{\left(\frac{\beta\sigma}{\lambda}\right)^2 + \epsilon_m^2} \tag{3.9}$$

Where E_ϕ gives the total error for the chosen pitch angle, ϕ; $\beta = 0.95r_{max} - 0.2r_{max} = 0.75r_{max}$ is the length of the acceptable radial range from which we can pick pitch angle, $\lambda = r_{out} - r_{in}$ is the length of the chosen stable region in the pitch angle vs radius graph, σ is the standard deviation of the mean pitch angle from the aforementioned stable region, and ϵ_m is the mode error associated with 2DFFT's discretization of pitch angle. Note that while we used a hard upper limit of $0.95r_{max}$ (unlike Davis et al. (2012), who used $0.9r_{max}$), we have very few pitch angles taken from stable regions that overlapped with $0.9r_{rmax}$ or greater (see Section 4.1.4).

[13]The GUI version of the overlay, *spiral_overlay.py*, developed by Erik Monson (currently an undergraduate in our research group), is in progress. See: `https://github.com/AGES-UARK/2dfft_utils/pull/1`.

4 Results

After analyzing the output of 11 model galaxies, which varied only in initial halo mass concentration (and subsequent but insignificant differences in mass), we find that, while the initial appearance of spiral arm structure and the exact manifestation of this structure differs between models, the overall evolution of pitch angle follows remarkably similar trends. Notably, while spiral arms do not last the entirety of the 3 Gyr period of evolution, this structure is reoccurring, with pitch angle remaining within a relatively narrow range throughout time. When we compare mean pitch angle to projected values of virial concentration, we find that a correlation is at best ambiguous.

4.1 Evolution of Models

4.1.1 General Spiral Structure

All models start out with an overall axisymmetric, circular structure resembling an S0 galaxy (one without any discernible spirals; see Figure 2.5). After taking on an elliptical shape, the disks start to form spiral structure at the edges, taking anywhere from 0.950 to 1.950 Gyr to produce clearly-defined bars and two distinct arms.

The values of γ and a_h have a noticeable effect on the amount of time it takes for spiral structure to form (Berlanga Medina et al., 2013, 2014, 2015). As γ increases and/or a_h decreases, it takes longer for spiral structure to form.

After initially forming, the spiral structure appears to remain stable for roughly 0.2 Gyr or more (Berlanga Medina et al., 2013, 2014, 2015). It eventually forms rings or polygons as the tips of the arms become less defined and start to blur into the opposite end of the bar from which they originated. The spiral structure may also dissipate entirely, leaving the galaxy dominated by a bar or pseudo-bar, especially in the later snapshots of the simulations. However, as demonstrated by panels (i), (m) and (p) in Figure 4.2, the spiral structure is recurring, usually coming back as a two-armed pattern. We see 2-4 periods of recurring spiral patterns during the total time observed.

The a1, b1, c1, c2, nfw1 and nfw2 models also see short-lived expressions of four-armed spirals or four-sided polygons, usually around 1.8-2.7 Gyr, and sometimes again around

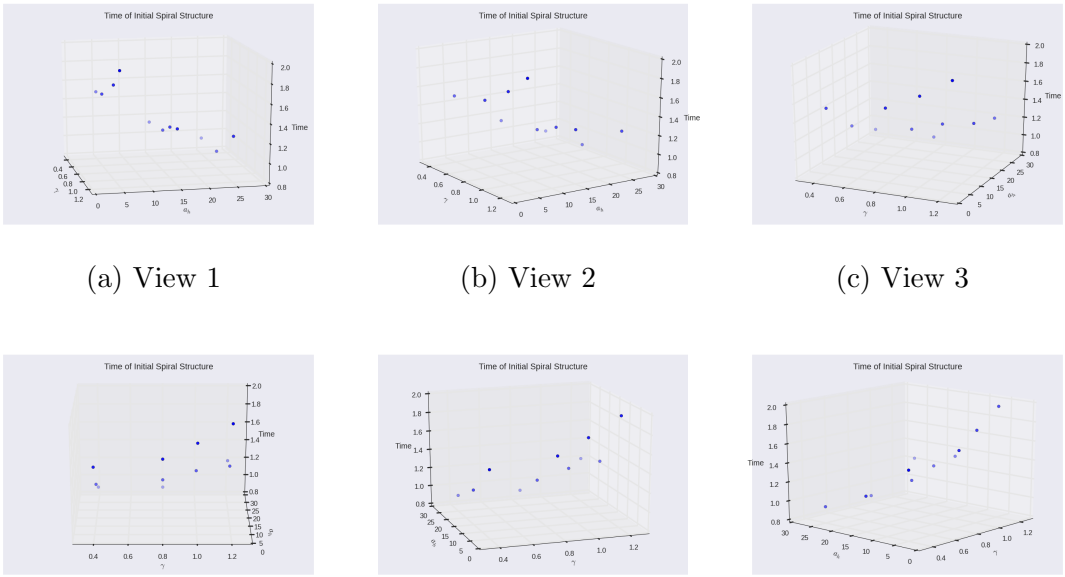

(a) View 1 (b) View 2 (c) View 3

(d) View 4 (e) View 5 (f) View 6

Figure 4.1: The initial appearance of spiral structure depends on γ and a_h. The larger the value of γ or the smaller the value of a_h, the longer it takes spiral structure to initially appear.

3 Gyr. Six-sided polygons may occur briefly but rarely, and odd modes never dominate enough to express three- or five-sided polygons or arms. The dominance of even modes, and in particular $m = 2$, is not surprising since the model template, GalactICS, is virtually guaranteed to produce a strong bar (see Section 3.1.1).

4.1.2 Pitch Angle

Due to some of the limitations and hurdles discussed in Section 3.3, we were not able to obtain pitch angle measurements for every single snapshot of the 61 total for each model. As seen in Figure 4.2, the shape of the spiral pattern is sometimes highly irregular, non-logarithmic, or not spiral at all.

It is difficult to predict *a priori* which points in time will successfully yield pitch angles for all models, so we opted to take as many measurements for all modes (except for $m = 1$), for as many snapshots as possible.

Taking pitch angle for all modes is important, as it is not always prudent to force a particular image of a galaxy into one mode category. For example, when one sees two large spurs that are not as large as the two main arms, the mode cannot be either two or four

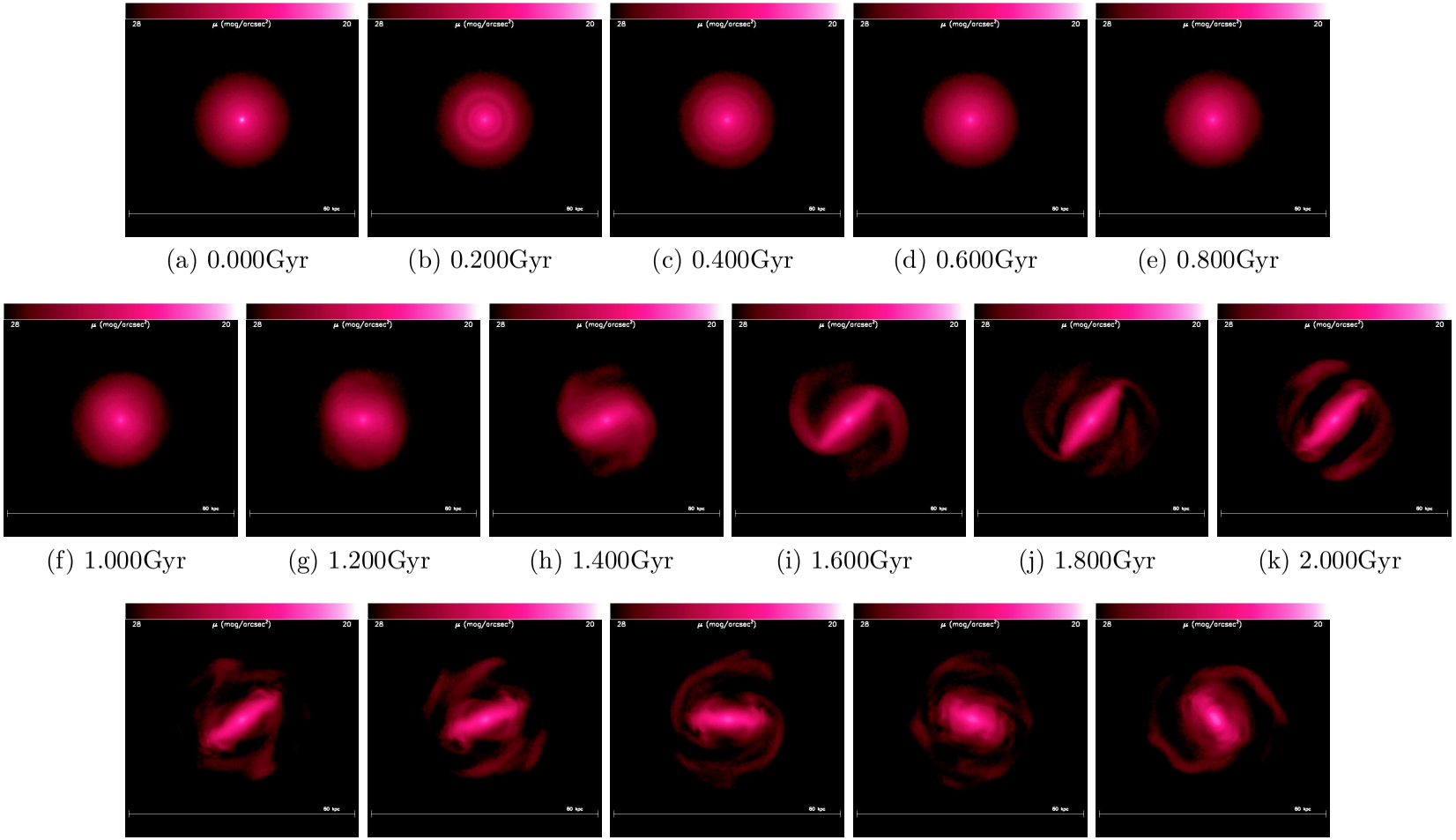

(a) 0.000Gyr (b) 0.200Gyr (c) 0.400Gyr (d) 0.600Gyr (e) 0.800Gyr

(f) 1.000Gyr (g) 1.200Gyr (h) 1.400Gyr (i) 1.600Gyr (j) 1.800Gyr (k) 2.000Gyr

(l) 2.200Gyr (m) 2.400Gyr (n) 2.600Gyr (o) 2.800Gyr (p) 3.000Gyr

Figure 4.2: Example of spiral structure evolution (model a1). After a period of stability, arms change into ring-like patterns or dissipate, then reform such that spiral structure periodically returns.

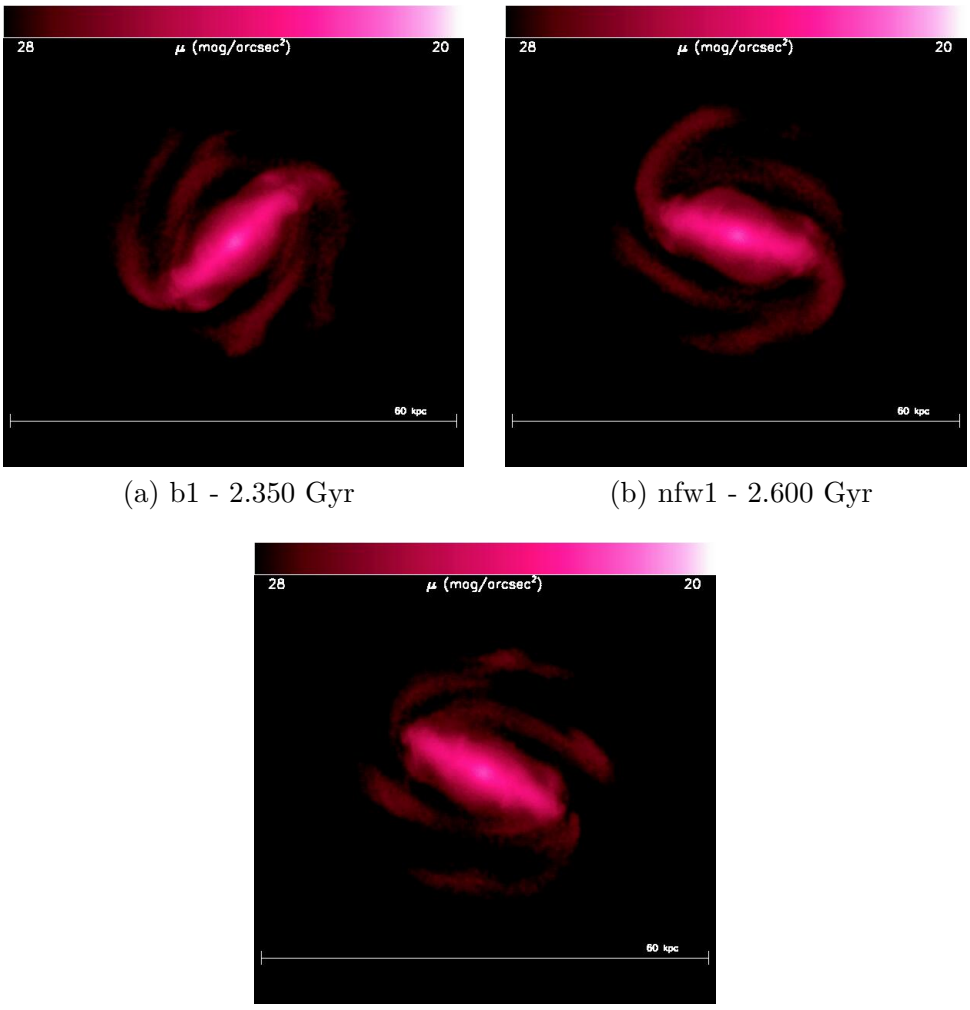

(a) b1 - 2.350 Gyr

(b) nfw1 - 2.600 Gyr

(c) c1 - 2.650 Gyr

Figure 4.3: Examples of snapshots in models b1, nfw1, and c1 where four-armed spiral structure was observed.

alone. When spurs/arms are not logarithmic or symmetric about the origin as assumed by 2DFFT, one mode cannot sufficiently describe the pattern. At the present time, we do not have a method for combining pitch angles from various modes to get one, "global" pitch angle, but nevertheless, we find it instructive to look at more than one mode to get idea of when a pitch angle measurement is more likely to be trustworthy (e.g., when various modes agree or have highly-overlapping stable regions in pitch angle vs. radius data).

Since even modes (and in particular $m = 2$) dominate both the images simulated from the N-body snapshots and the 2DFFT data, we initially focused on modes $m = 2, 4, 6$, but later acquired data for the odd modes after some of the 2DFFT Utilities tools were updated and pitch angle measurement became more efficient[1]. As a result, there are subtle (though largely insignificant) differences in the even and odd mode datasets. For these reasons, we present the two datasets separately and focus on the $m = 2$ mode for detailed analysis.

Pitch angle stays remarkably stable over time. As seen in Figures 4.4, all modes tend to jump around in the first 0.3-0.5 Gyr or so, then go through periodic eras of relative stability followed by instability. This is not surprising given the overall patterns of evolution we see in the snapshot images of our model. We do see some decrease in pitch angle over the eras of stability, with jumping around.

The snapshots with negative pitch angles are instances at which 2DFFT "found" spiral arms winding in the counter clockwise direction (instead of clockwise, as they do during most of the evolutionary period). Interestingly, the absolute values of the negative pitch angles usually remain close to the values of the positive pitch angles.

On the whole, pitch angle does not differ greatly between models. Figures 4.5, 4.6, 4.7 and 4.8 show pitch angle evolution for the a, b, nfw and c group models, respectively. The $m = 2$ mode is the most stable overall, showing less variation than all other modes. In general, smaller modes (which were easier to measure, and have more data points as a result), show less variation than larger modes, and less error as well. Roughly speaking, pitch angle absolute values tend to stay between 20°-30°, and tend to become larger as mode values increase.

The distribution of pitch angles over the entire simulation period reflects this, showing a strong peak for $m = 2$ for nearly all models. Figure 4.9 shows that as even mode number

[1]Erik Monson updated some of these tools and took measurements for modes $m = 3, 5$ using these updates, while the author took measurements for modes $m = 2, 4, 6$ using an preliminary version of 2DFFT Utilities. Therefore the odd mode dataset is slightly different from the even mode dataset.

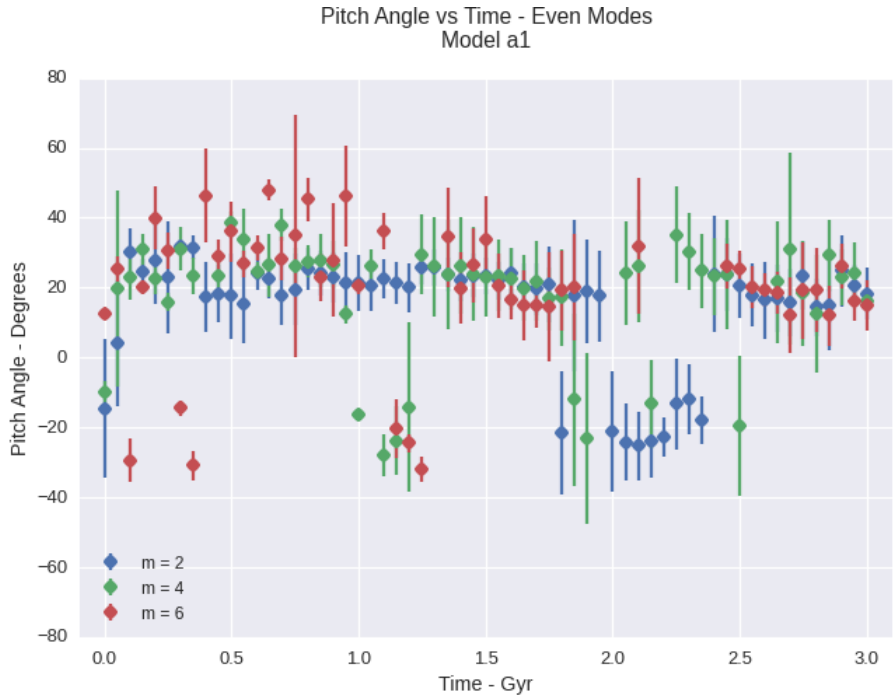

(a) Even Modes - a1

(b) Odd Modes - a1

Figure 4.4: An example of pitch angle evolution over time (model a1). Since even modes dominate all models (in particular $m = 2$ and $m = 4$ to some extent) and for visual clarity, we show even and odd modes separately.

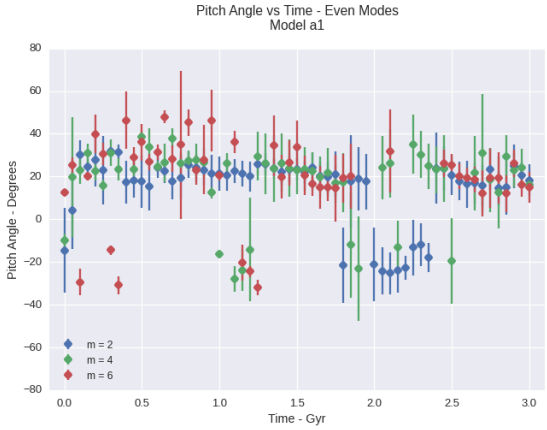

(a) Even Modes - a1

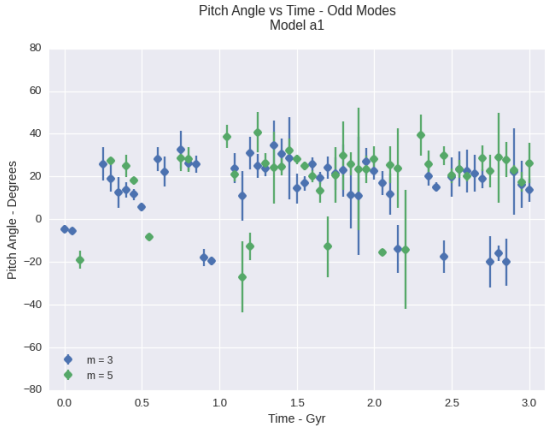

(b) Odd Modes - a1

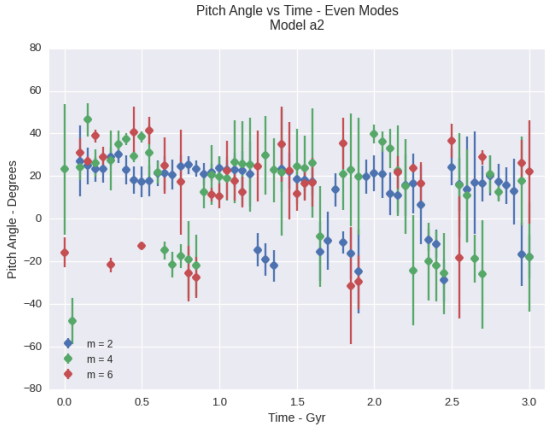

(c) Even Modes - a2

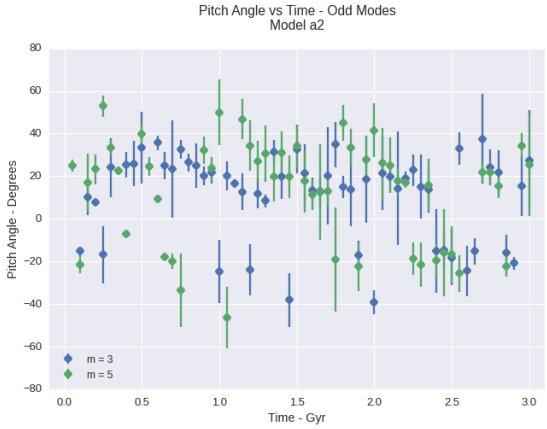

(d) Odd Modes - a2

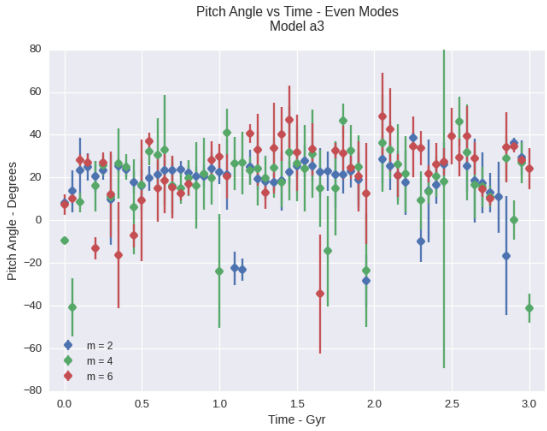

(e) Even Modes - a3

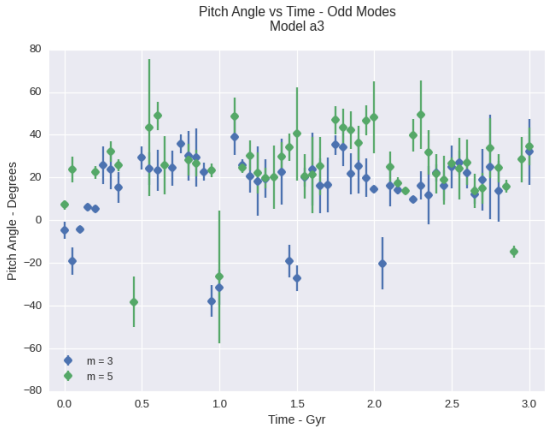

(f) Odd Modes - a3

Figure 4.5: Pitch angle evolution over time for models a1, a2, and a3.

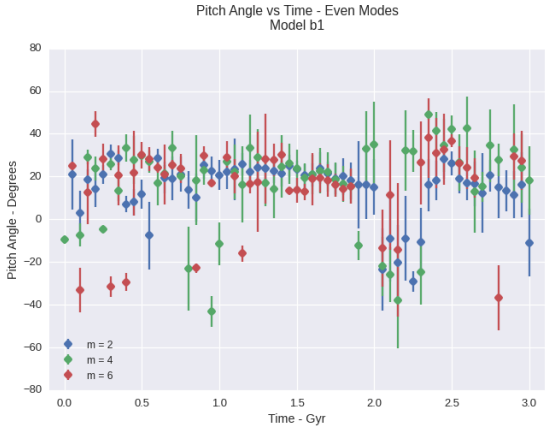

(a) Even Modes - b1

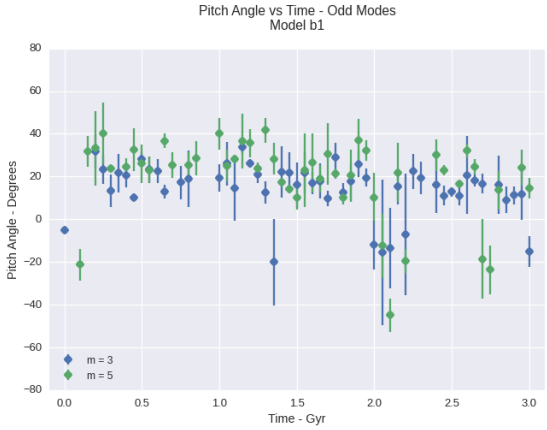

(b) Odd Modes - b1

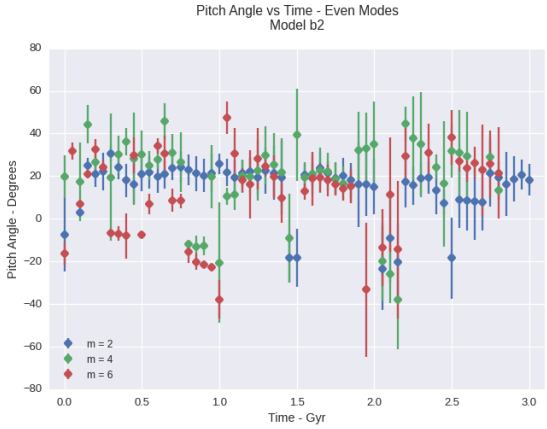

(c) Even Modes - b2

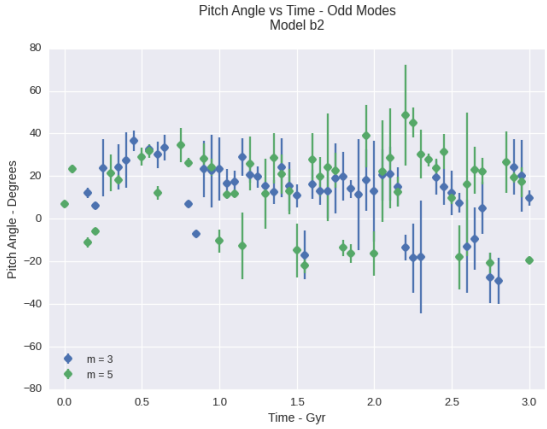

(d) Odd Modes - b2

(e) Even Modes - b3

(f) Odd Modes - b3

Figure 4.6: Pitch angle evolution over time for models b1, b2, and b3.

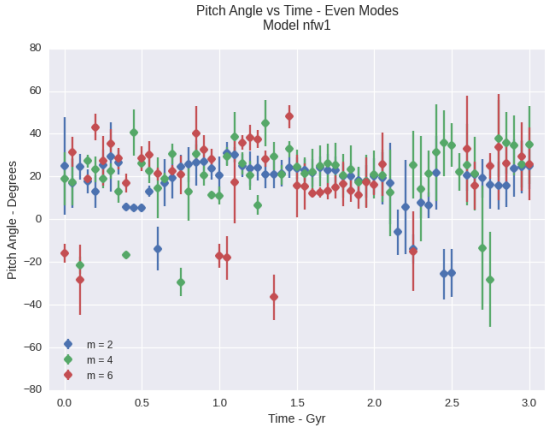

(a) Even Modes - nfw1

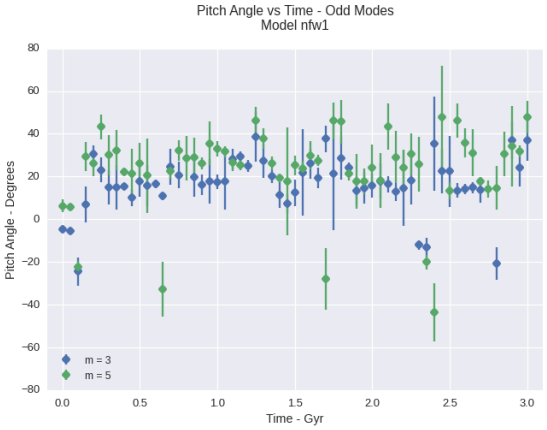

(b) Odd Modes - nfw1

(c) Even Modes - nfw2

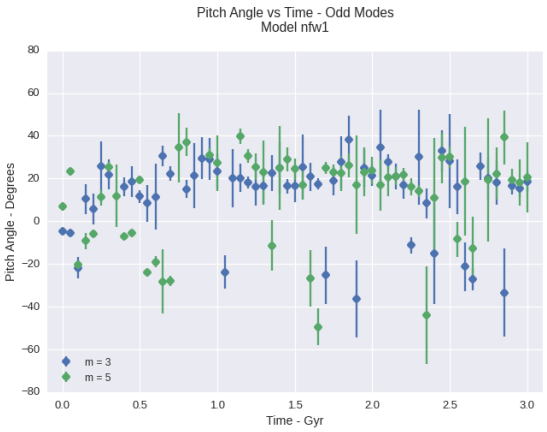

(d) Odd Modes - nfw2

Figure 4.7: Pitch angle evolution over time for models nfw1 and nfw2.

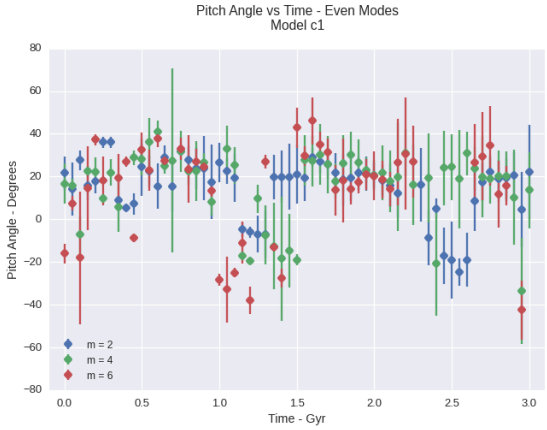

(a) Even Modes - c1

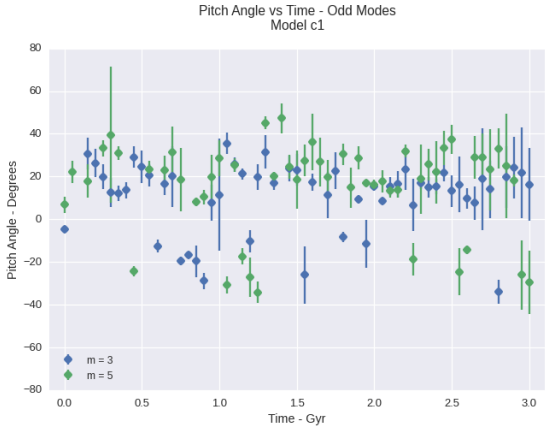

(b) Odd Modes - c1

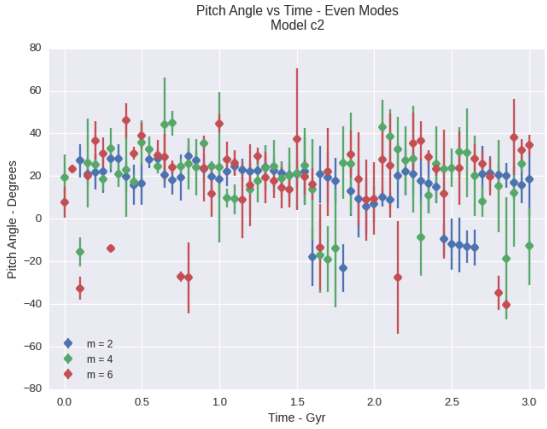

(c) Even Modes - c2

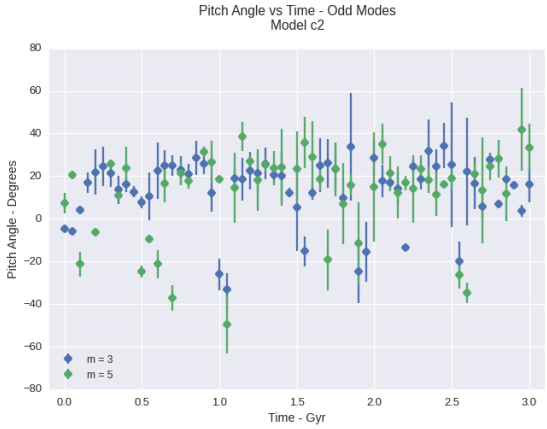

(d) Odd Modes - c2

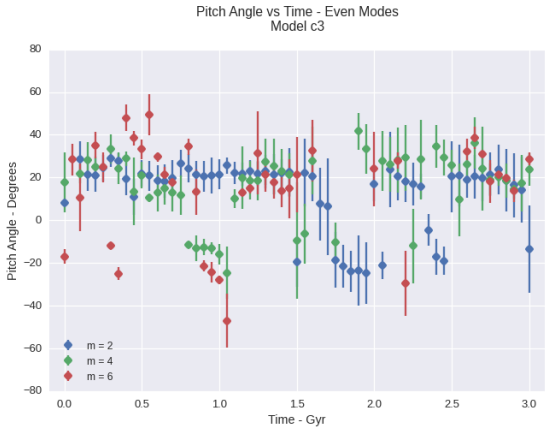

(e) Even Modes - c3

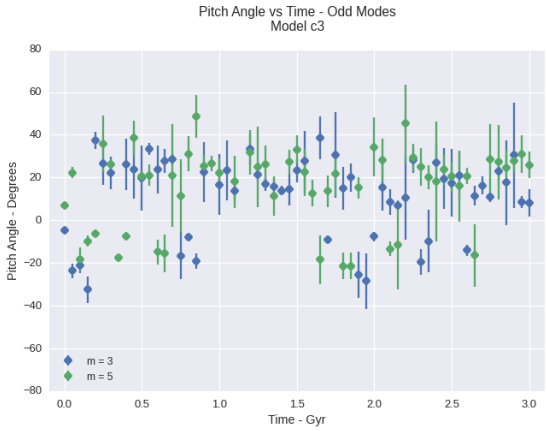

(f) Odd Modes - c3

Figure 4.8: Pitch angle evolution over time for models c1, c2, and c3.

increases, the distribution spreads out and the peak moves to greater pitch angle values.

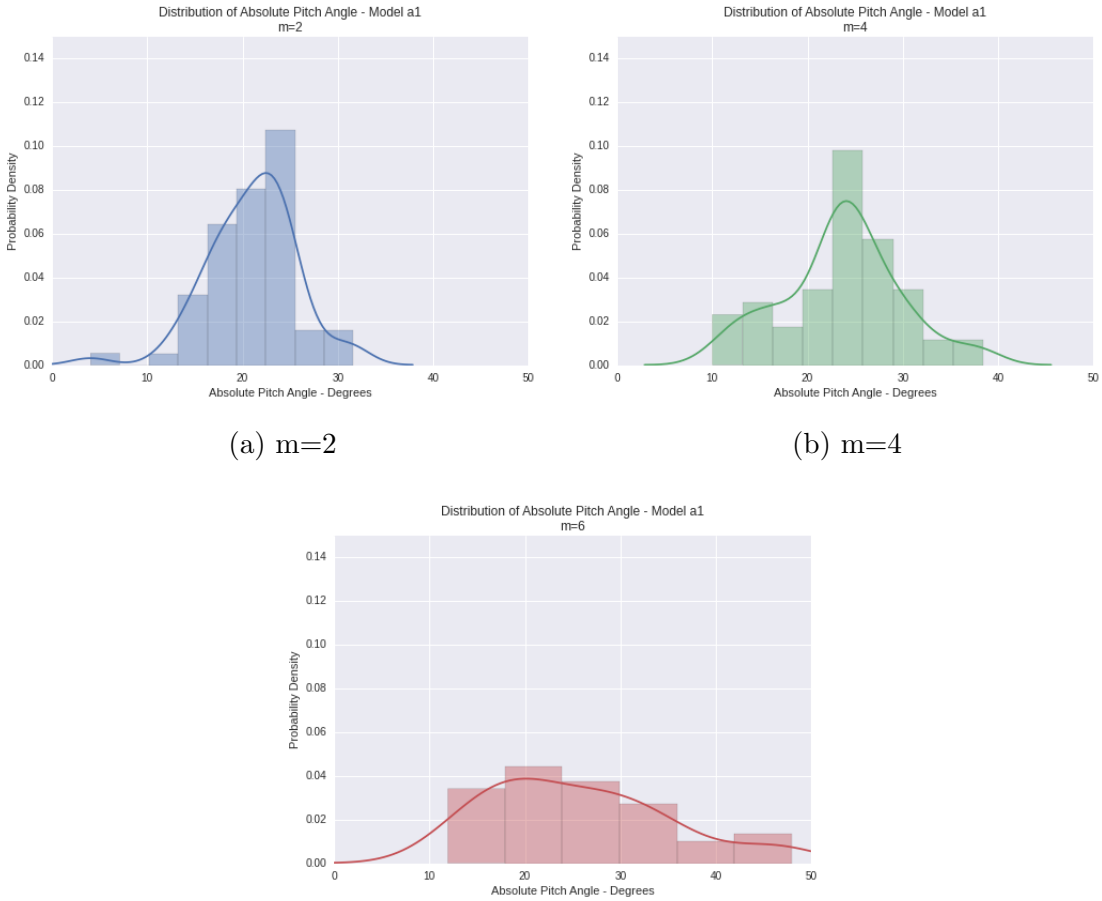

(a) m=2

(b) m=4

(c) m=6

Figure 4.9: Pitch angle distribution for even modes of model a1. A kernel density estimation (KDE) is used to approximate the probability distribution function (PDF) of pitch angle, assuming a normal distribution. Bin width was chosen and PDF fitted automatically using the *distplot* function of the Python statistical visualization library, Seaborn (Waskom et al., 2015).

Odd modes do not necessarily follow the same trend. For a given model, the $m = 5$ mode does generally have a peak that is shifted to a larger pitch angle than $m = 3$, but as Figure 4.10 shows, the distribution is not necessarily flatter. Overall, the $m = 2$ and $m = 4$ have much stronger peaks than all other modes (3, 5 and 6), suggesting that 2DFFT was consistently picking up stronger signals from the former.

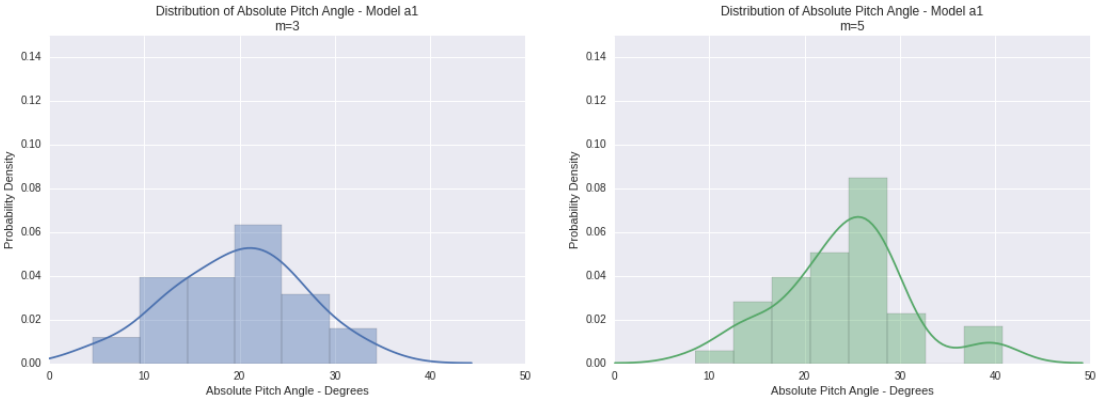

(a) m=3 (b) m=5

Figure 4.10: Pitch angle distribution for odd modes of model a1. The sharp peak for $m = 5$ is unusually high—all other models have generally flatter distributions.

4.1.3 Eras of Stable Pitch Angle

Since we cannot pick any regular sampling of snapshots and be guaranteed to have pitch angle measurements for all models and all modes, we decided to try and pick out periods of time over which pitch angle remained relatively stable in the $m = 2$ mode for all models. We only looked at $m = 2$ since other modes have significantly less measured pitch angles and exhibit less stability over time. We wanted to find periods of time during which all the models had overlapping eras of stability in order to compare likely virial concentration values with pitch angle.

To pick out eras of stability, we adapted our *slope_change.py* tool from 2DFFT Utilities (see 3.3.2) to highlight periods of time where pitch angles for consecutive snapshots did not change by more than a threshold amount, which we varied from $5°/snapshot$ to $6°/snapshot$ (where 1 snapshot = 0.05 Gyr). The eras of stability had to be at least 3 snapshots long, or 5% of the total 3 Gyr period.

As seen in Figure 4.12, it was not possible to find common eras of stability for all models that lasted less than 1 Gyr or more. This was due to a combination of missing pitch angle measurements (for snapshots with highly-irregular or non-logarithmic spiral structure) as well as periodic instability. The only way to pick out more common eras would be to accept higher rates of change as stable (larger than $6°/snapshot$). Since the only possible common eras of stability sample from such a large fraction of the total evolutionary period, we decided to compare likely virial concentration values to the mean pitch angle over the

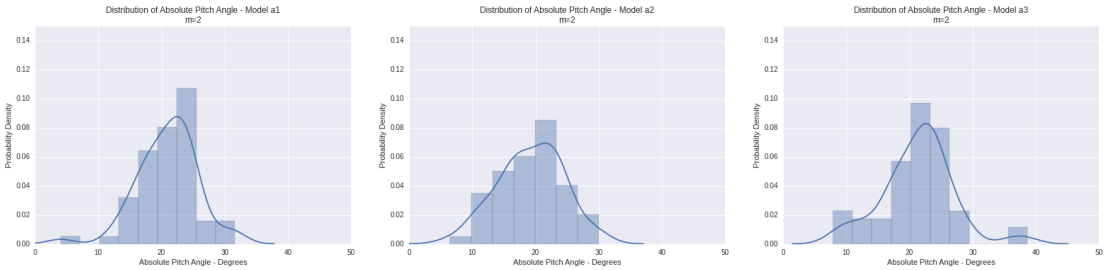

(a) a1

(b) a2

(c) a3

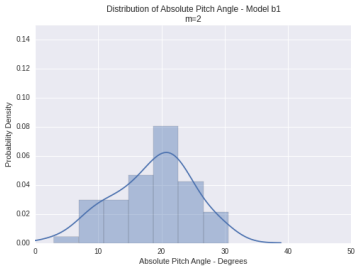

(d) b1

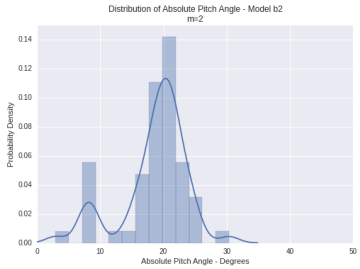

(e) b2

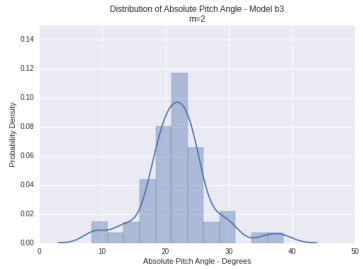

(f) b3

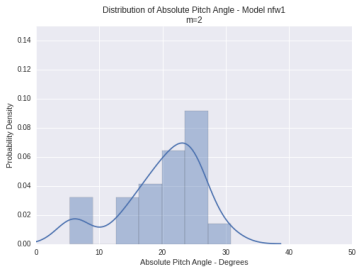

(g) nfw1

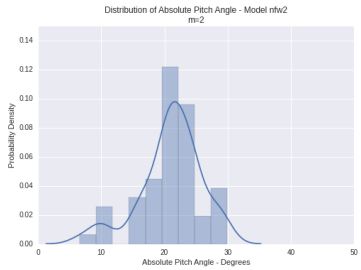

(h) nfw2

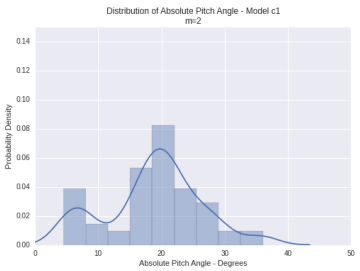

(i) c1

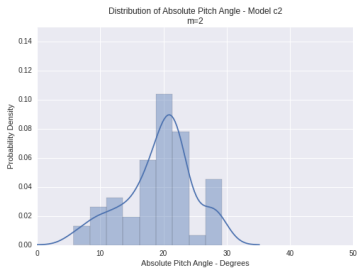

(j) c2

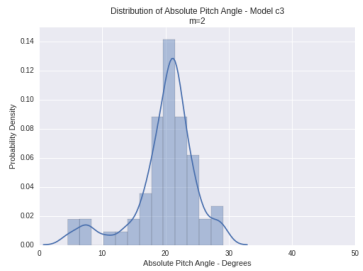

(k) c3

Figure 4.11: Pitch angle distribution for $m = 2$, all models.

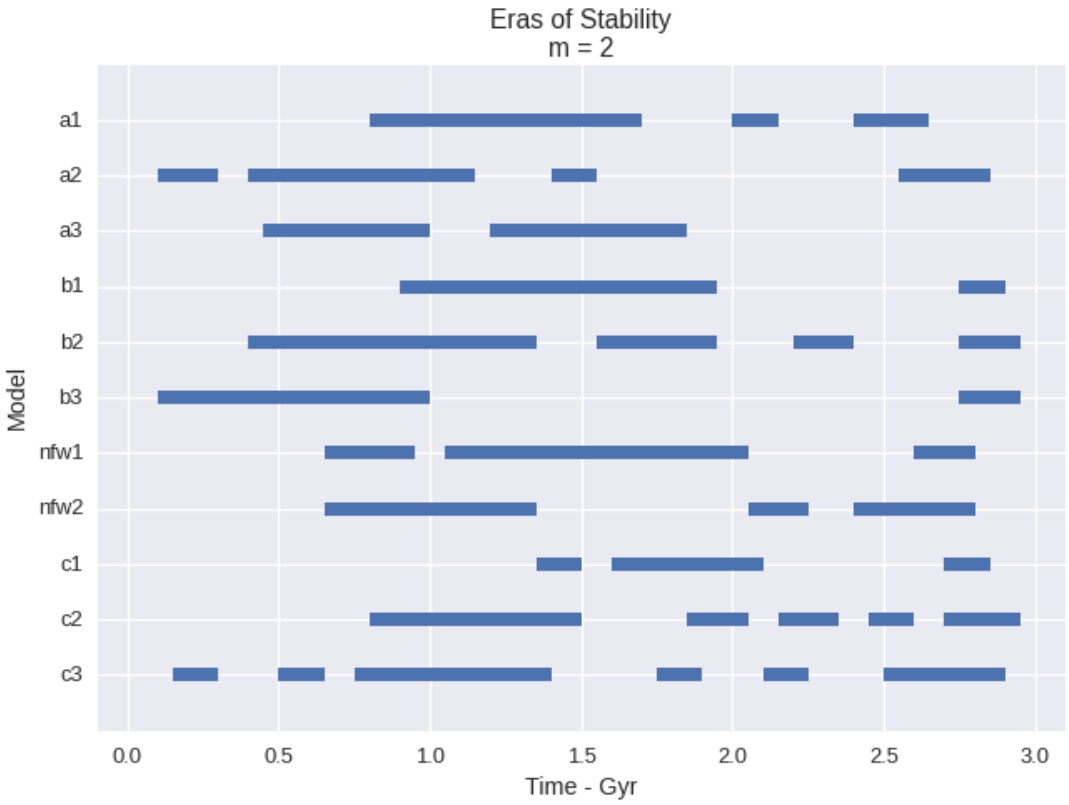

Figure 4.12: Eras of pitch angle stability for $m = 2$, all models. The threshold for instability is $6°/snapshot$ or $120°$/Gyr.

entire 3 Gyr period instead.

4.1.4 Regions of Stable Pitch Angle

When measuring pitch angle, two of our selection criteria were the location and length of the stable region in pitch angle vs. radius graphs. We based this on the idea that the stable region is physically significant—it must not be too small, so that it covers some minimum radial extent, but it must also not be part of the bar, nor be narrow while laying in the outer 5-10% of the disk.

We looked at the location and size of the stable region with respect to the total disk radius (r_{out}) for $m = 2$ at every time for which we measured a viable pitch angle. As the dominant mode, perhaps it is unsurprising that $m = 2$ yielded the most viable pitch angle measurements in all models. Since $m = 2$ pitch angles cover most of the 3 Gyr simulation period, we choose this mode to focus on for this aspect of analysis.

Figure 4.13 shows stable region evolution for one model, a1, and marks the mean value for the center of all the regions. As seen in Figure ,we found that most of our pitch angles were covering much the same radial extents over the entire simulation period. This means that, as the disk grew, making r_{out} larger, the regions with the most stable pitch angles tended to move away from the center at a proportionate rate.

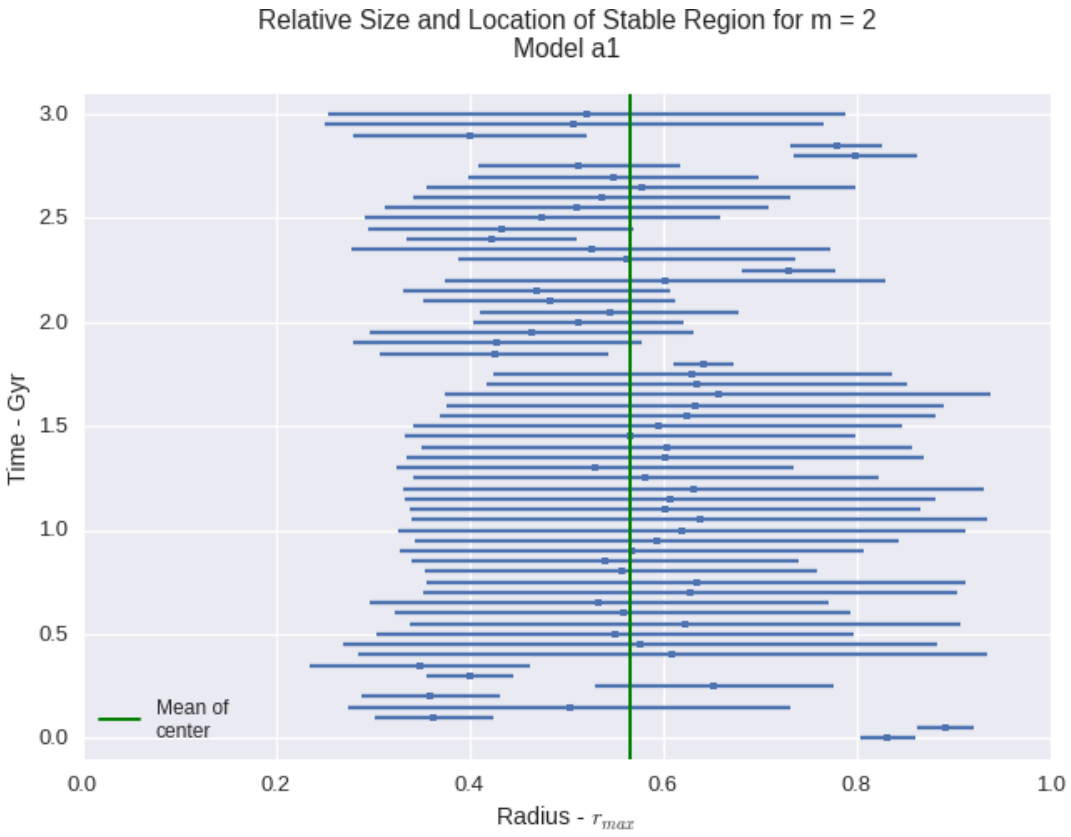

Figure 4.13: The evolution of the stable region over time for model a1 and mode $m = 2$. The blue dots show the centers of the stable regions, and the green vertical line shows the center mean.

We cannot compare pitch angles across all models for all times, but we can identify overlapping periods of time during which all models have reasonably reliable pitch angle measurements. We have done so, and describe these results below.

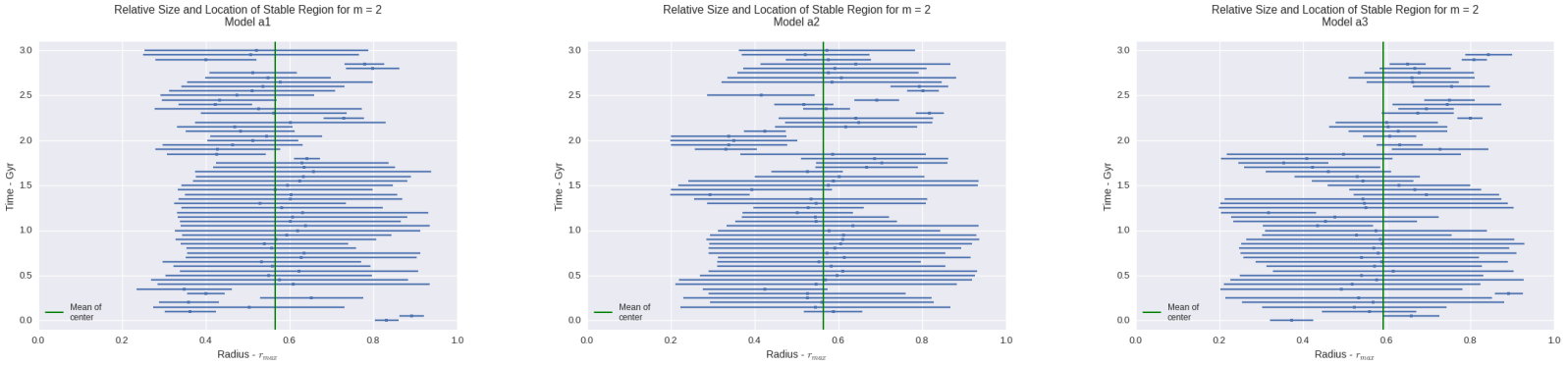

(a) Stable Regions - a1

(b) Stable Regions - a2

(c) Stable Regions - a3

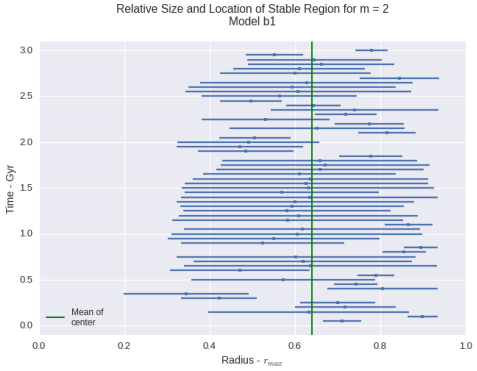

(d) Stable Regions - b1

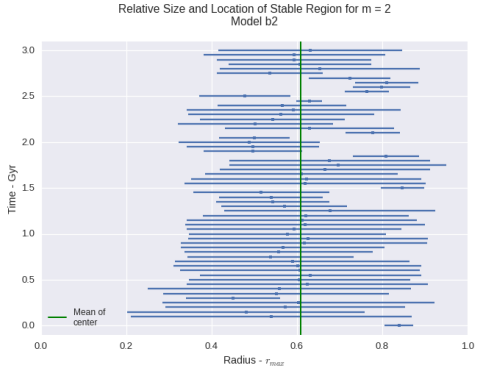

(e) Stable Regions - b2

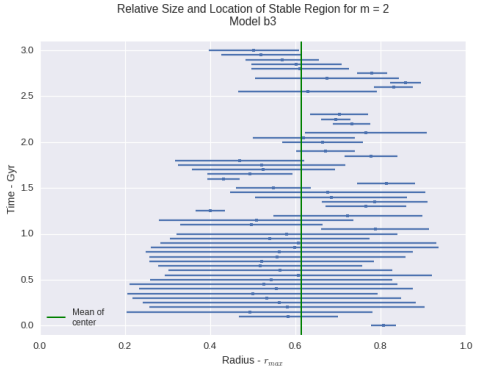

(f) Stable Regions - b3

Figure 4.14: Evolution of stable region location and length over time for $m = 2$, models a1, a2, a3, b1, b2, b3.

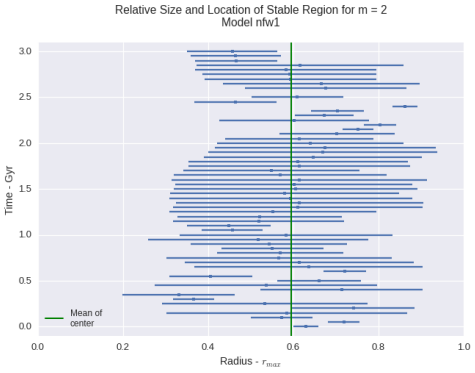

(a) Stable Regions - nfw1

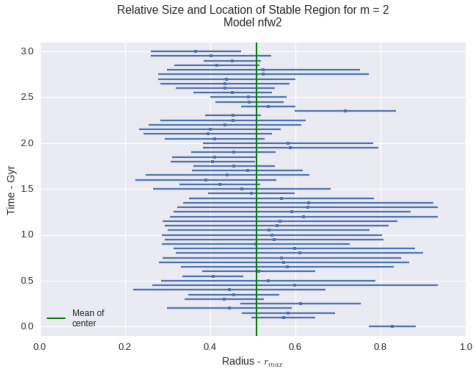

(b) Stable Regions - nfw2

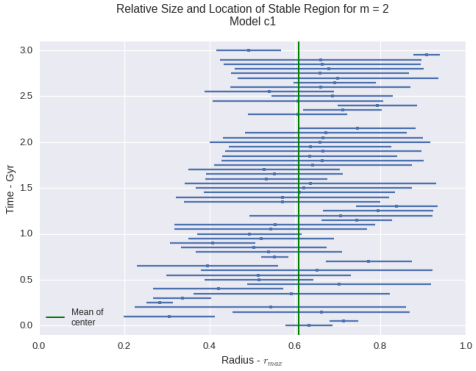

(c) Stable Regions - c1

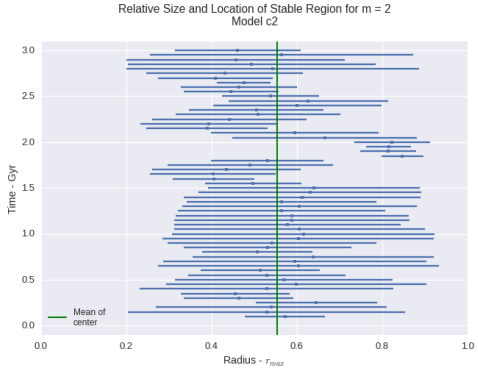

(d) Stable Regions - c2

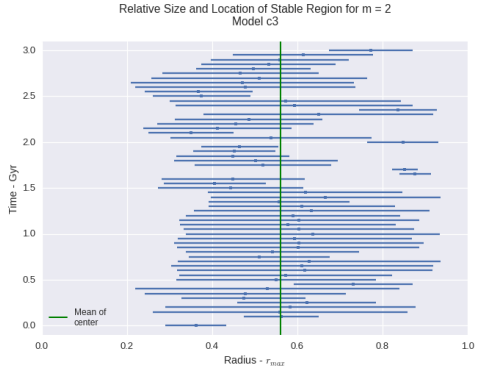

(e) Stable Regions - c3

Figure 4.15: Evolution of stable region location and length over time for $m = 2$, models nfw1, nfw2, c1, c2, c3.

4.2 Pitch Angle vs Virial Concentration

Since we were not able to isolate regions of time during which pitch angle was stable enough to compare across all models, we choose to take the absolute value of every available pitch angle measurement for mode $m = 2$, and take means for every model. Then, since we did not have direct measurements for virial concentration, we took likely R_s values from Widrow et al. (2008) and used Equations 3.7 and 3.8 to calculate projected c_{vir}. This data can be found in Table 4.1.

As seen in Figure 4.16, there is a suggestion of a correlation between virial concentration of the dark matter halo and the absolute value of the mean pitch angle over time, specifically that of larger c_{vir} values corresponding to smaller $|P|$. However, the projected values of virial concentration and the measured values of pitch angle lie in a wide range. As is evident in the linear regression fit of the data (Figure 4.17), the sample size is too small to make a prediction about the behavior of these two parameters outside the narrow range of 18.5884° to 21.9232° for absolute pitch angle. The Pearson coefficient of correlation, which corresponds to high and low correlation at absolute values of one and zero, respectively, is ambiguous at -0.4900.

Model	$\lvert P_{mean}\rvert$	$\lvert P_{median}\rvert$	$\sigma_{\lvert P\rvert}$	Min. c_{vir}	Max. c_{vir}
a1	20.9548	21.2073	4.6540	25.0000	65.0000
a2	19.2275	19.6180	5.0712	8.3333	21.6667
a3	21.3375	21.9468	5.6318	5.0000	13.0000
b1	18.6141	19.7759	6.1312	41.6667	108.3333
b2	18.5884	19.6872	5.1841	11.1111	28.8889
b3	21.9232	21.8253	5.2984	6.6667	17.3333
nfw1	19.8652	20.9102	6.4326	40.0000	104.0000
nfw2	20.9770	21.2579	4.8880	13.3333	34.6667
c1	18.7756	19.1808	7.4907	50.0000	130.0000
c2	19.2954	20.4696	5.4082	16.6667	43.3333
c3	19.9811	20.9076	4.8755	10.0000	26.0000

Table 4.1: Pitch angle statistics for all models, $m = 2$. Mean and median absolute pitch angles are very close, so we opted to use the means to compare against projected c_{vir}. Projected minimum and maximum c_{vir} values are calculated using likely values of R_s and Equations 3.7 and 3.8. See Section 3.1 for more details, and Table 3.1 for corresponding γ and a_h values.

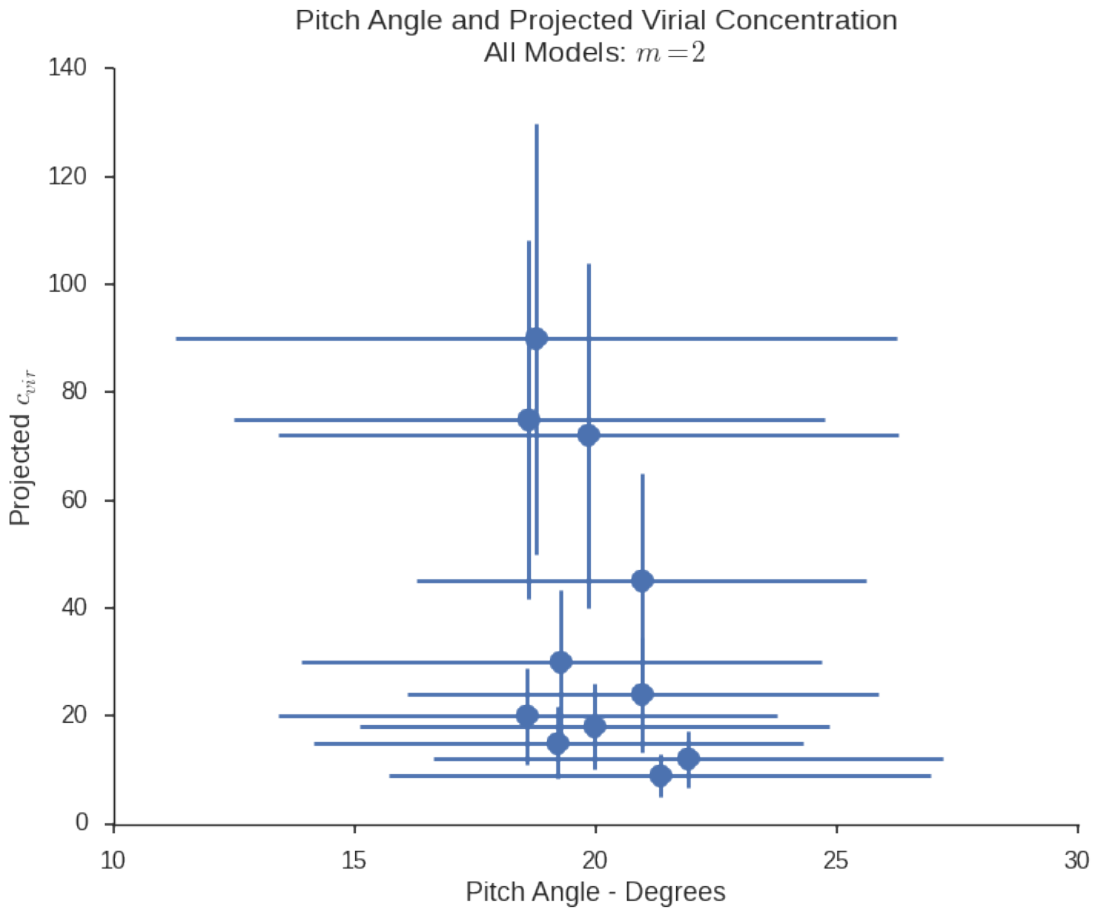

Figure 4.16: $|P_{mean}|$ vs projected c_{vir} for $m = 2$. Data same as 4.1. The midpoint of projected c_{vir} values is plotted with respect to the y-axis, while the projected range is indicated by the vertical error bars. Mean values for absolute pitch angles have horizontal error bars indicating the standard deviation. There is no strong correlation between pitch angle and virial concentration, but a relationship cannot be ruled out, either.

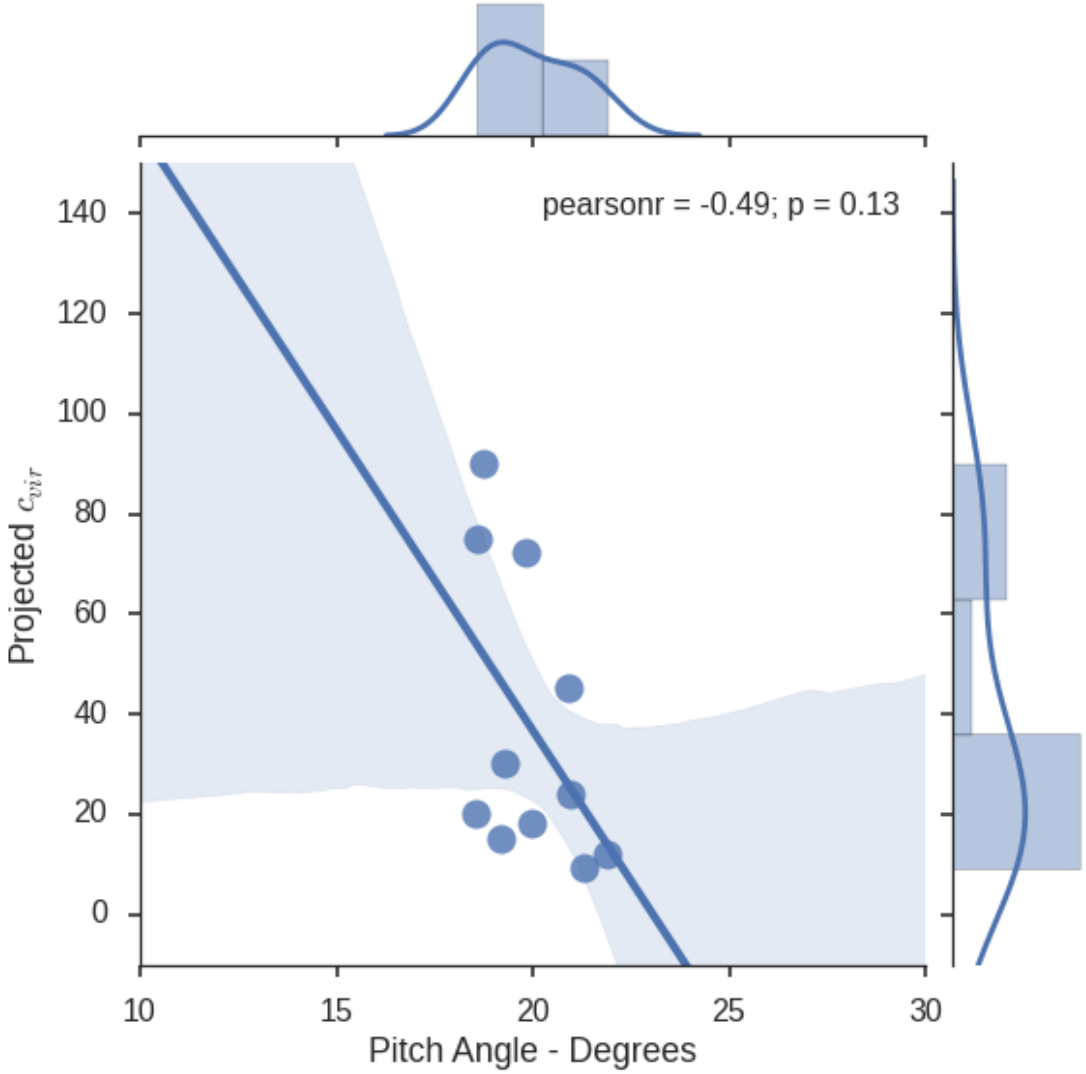

Figure 4.17: Same data as and limits as in Figure 4.16, but with a linear regression fit and marginal distributions, as well as a Pearson correlation coefficient and the two-tailed p-value for testing non-correlation (the last two computed with SciPy's *stats.pearsonr* function). The linear regression fit suggests a correlation between larger virial concentration and smaller pitch angle, but the fit is not tight enough to support this conclusion. The Pearson correlation coefficient gives ambiguous results, and the p-value is not reliable for small sample sizes. The small sample size is reflected in the marginal distributions for both pitch angle and virial concentration.

5 Discussion

5.1 Testing Theories and Predictions

As discussed in Chapter 2, there are several aspects that one could test when trying to differentiate between theories of spiral structure and the influence of matter concentration (including dark matter) on the evolution of the disk. It is not within the scope of this work to test all of them, but there are a few we can comment on per our results.

5.1.1 Longevity of Spiral Patterns

Most spiral structure formation theories predict the longevity of the spiral arms. Density wave theory posits that spiral structure is stable over time due to the standing density wave. Stochastic, self-propagating star formation and the manifold theory agree with longevity of spiral structure as long as there is sufficient material in the disk to power their respective mechanisms. Swing amplification theory states that spiral arms are short-lived since they tend to wind down after some time, but only the recurrent picture of swing amplification/density waves allows for periodic spiral patterns.

Our results find that spiral arms are not long-lived, with visible patterns lasting, on average, a few hundred Myr. However, they are recurring, which suggests that something like periodic swing amplification could be responsible for this structure, or that transient structure is being regenerated.

5.1.2 Pitch Angle

Since swing amplification theory and SSPSF depend on differential rotation, they predict that pitch angle will get smaller over time due to winding of the spiral arms. Only the density wave and manifold theories make specific predictions about pitch angle beyond this–they anticipate specific forms based on other aspects of galactic structure.

Density wave theory predicts that higher levels of central baryonic (not necessarily dark matter) mass lead to smaller pitch angles, in particular central bulge mass. The density of gas in the disk also plays a role. The dark matter is a small fraction of the central bulge mass and (assuming a spherical distribution) should not contribute to the disk density. There

is ambiguity about the role of dark matter concentration in density wave theory, but some argue for the same general trend. The manifold theory predicts that stronger bars and falling (instead of flat or rising) rotation curves lead to stronger spiral arms.

We primarily looked at a possible relationship between dark matter virial concentration and pitch angle, so we did not investigate other aspects of our model galaxies. We found that a large range of projected virial concentration values produced very little variation in pitch angle. The fact that the dark matter concentration has, at best, a very weak correlation with spiral arm pitch angle is compatible with the density wave theory.

We also looked at how pitch angle evolved over time and found that it remained relatively stable over most of the 3 Gyr period of evolution, in contrast to findings by Grand et al. (2013); Michikoshi & Kokubo (2014) (although the former did not sample the simulation time period and the later looked only at localized spiral structure, and did not evolve an entire galaxy).

5.1.3 What We Cannot Test

Its worthwhile to note what aspects of spiral arm formation we do not purport to test. We can't comment on any processes involving gas or star formation since our model was gravity-only. We did not measure bar strength or other aspects of the central part of the galaxy which have previously been looked at in conjunction with pitch angle and/or dark matter concentration. We also cannot discern between the density theory and manifold theory in terms of particle movement with respect to the arms.

5.2 Summary

Though our results cannot rule out a relationship between virial concentration and pitch angle, we can take away a few key points about the evolution of spiral structure and that of barred spiral galaxies in particular. We see transient but reoccurring patterns in the disk. The spiral arms are both qualitatively and quantitatively similar in each iteration. The pitch angle distribution in final $c_{vir} - |P|$ data is rather narrow compared to observational data in the literature. As a result, any linear fit between increasing virial concentration and decreasing, absolute pitch angle is ambiguous, neither supporting nor rejecting this particular prediction. These results do not sufficiently test any one theory, but they do support one that predicts periodic, recurring spiral arms within a relatively narrow range of pitch angles

over time.

Bibliography

Astropy Collaboration, Robitaille, T. P., Tollerud, E. J., et al. 2013, , 558, A33

Athanassoula, E., Romero-Gómez, M., Bosma, A., & Masdemont, J. J. 2009a, , 400, 1706

—. 2010, , 407, 1433

Athanassoula, E., Romero-Gómez, M., & Masdemont, J. J. 2009b, , 394, 67

AURA. 2015, AURA: Association of Universities for Research in Astronomy

Berlanga Medina, J., Berrier, J. C., Kennefick, D., & Arkansas Galaxy Evolution Survey. 2015, in American Astronomical Society Meeting Abstracts, Vol. 225, American Astronomical Society Meeting Abstracts, 250.11

Berlanga Medina, J., Berrier, J. C., Hartley, M., et al. 2013, in American Astronomical Society Meeting Abstracts, Vol. 221, American Astronomical Society Meeting Abstracts #221, 146.24

Berlanga Medina, J., Berrier, J., Hartley, M., et al. 2014, in American Astronomical Society Meeting Abstracts, Vol. 223, American Astronomical Society Meeting Abstracts #223, 453.20

Berrier, J. C., Davis, B. L., Kennefick, D., et al. 2013, , 769, 132

Carroll, B. W., & Ostlie, D. A. 2006, An Introduction to Modern Astrophysics and cosmology

Davis, B. L., Berrier, J. C., Shields, D. W., et al. 2012, , 199, 33

Davis, B. L., Berrier, J. C., Johns, L., et al. 2014, , 789, 124

Davis, B. L., Kennefick, D., Kennefick, J., et al. 2015, , 802, L13

Gallazzi, A., Charlot, S., Brinchmann, J., White, S. D. M., & Tremonti, C. A. 2005, , 362, 41

Gebhardt, K., Bender, R., Bower, G., et al. 2000, , 539, L13

Gerola, H., & Seiden, P. E. 1978, , 223, 129

Goldreich, P., & Lynden-Bell, D. 1965, , 130, 125

Grand, R. J. J., Kawata, D., & Cropper, M. 2012a, , 426, 167

—. 2012b, , 421, 1529

—. 2013, , 553, A77

Gültekin, K., Richstone, D. O., Gebhardt, K., et al. 2009, , 698, 198

Heggie, D., & Hut, P. 2003, The Gravitational Million-Body Problem: A Multidisciplinary Approach to Star Cluster Dynamics

HST, & ESA. 2015, Hubble Space Telescope

Hubble, E. P. 1926, , 64, 321

Jetley, P., Gioachin, F., Mendes, C., Kale, L., & Quinn, T. 2008, in Parallel and Distributed Processing, 2008. IPDPS 2008. IEEE International Symposium on, 1–12

Kormendy, J., & Richstone, D. 1995, , 33, 581

Kuijken, K., & Dubinski, J. 1995, , 277, 1341

Lin, C. C., & Shu, F. H. 1964, , 140, 646

—. 1966, Proceedings of the National Academy of Science, 55, 229

Lin, C. C., & Shu, F. H. 1967, in IAU Symposium, Vol. 31, Radio Astronomy and the Galactic System, ed. H. van Woerden, 313

Marconi, A., & Hunt, L. K. 2003, , 589, L21

McConnell, N. J., & Ma, C.-P. 2013, , 764, 184

Menon, H., Wesolowski, L., Zheng, G., et al. 2015, Computational Astrophysics and Cosmology, 2, 1

Merritt, D., & Ferrarese, L. 2001, , 547, 140

Michikoshi, S., & Kokubo, E. 2014, , 787, 174

N-Body Shop. 2015, Tipsy, Online, [Online; accessed 23-Oct-2015]

NASA. 2015, NASA

Navarro, J. F., Frenk, C. S., & White, S. D. M. 1995, , 275, 56

—. 1996, , 462, 563

—. 1997, , 490, 493

Seiden, P. E., & Gerola, H. 1979, , 233, 56

Seigar, M. S. 2005, , 361, L20

Seigar, M. S., & Berrier, J. 2011, Galaxy Rotation Curves in the Context of LambdaCDM Cosmology, 77–102

Seigar, M. S., Block, D. L., Puerari, I., Chorney, N. E., & James, P. A. 2005, , 359, 1065

Seigar, M. S., Bullock, J. S., Barth, A. J., & Ho, L. C. 2006, , 645, 1012

Seigar, M. S., Davis, B. L., Berrier, J., & Kennefick, D. 2014, , 795, 90

Seigar, M. S., Kennefick, D., Kennefick, J., & Lacy, C. H. S. 2008, , 678, L93

Sellwood, J. A. 2011, , 410, 1637

Sellwood, J. A., & Carlberg, R. G. 1984, , 282, 61

—. 2014, , 785, 137

Smith, D. H. 1987, , 74, 136

Springel, V. 2005, , 364, 1105

SSC, & Caltech. 2010, SSC: Spitzer Science Center

STScI. 2015, Space Telescope Science Institute

Toomre, A. 1981, in Structure and Evolution of Normal Galaxies, ed. S. M. Fall & D. Lynden-Bell, 111–136

Tremaine, S., Gebhardt, K., Bender, R., et al. 2002, , 574, 740

Treuthardt, P., Seigar, M. S., Sierra, A. D., et al. 2012, , 423, 3118

Waskom, M., Botvinnik, O., Hobson, P., et al. 2015, seaborn: v0.6.0 (June 2015), doi:10.5281/zenodo.19108

Whittle, M. 2002-2005, Logarithmic Spirals: Constant Pitch Angle, Online, [Online; accessed 11-May-2015]

Widrow, L. M., Pym, B., & Dubinski, J. 2008, , 679, 1239

Wikipedia. 2014a, Flocculent spiral galaxy — Wikipedia, The Free Encyclopedia, [Online; accessed 21-September-2015]

—. 2014b, Grand design spiral galaxy — Wikipedia, The Free Encyclopedia, [Online; accessed 21-September-2015]

—. 2015a, Barred spiral galaxy — Wikipedia, The Free Encyclopedia, [Online; accessed 21-September-2015]

—. 2015b, Density wave theory — Wikipedia, The Free Encyclopedia, [Online; accessed 7-October-2015]

—. 2015c, Galaxy morphological classification — Wikipedia, The Free Encyclopedia, [Online; accessed 29-September-2015]

—. 2015d, Hubble sequence — Wikipedia, The Free Encyclopedia, [Online; accessed 21-September-2015]

—. 2015e, Irregular galaxy — Wikipedia, The Free Encyclopedia, [Online; accessed 29-September-2015]